Spatially resolved thermoreflectance techniques for thermal conductivity measurements from the nanoscale to the mesoscale (EP)

David H. Olson (iD), Jeffrey L. Braun (iD), and Patrick E. Hopkins (iD)

COLLECTIONS

EP   This paper was selected as an Editor's Pick

View Online   Export Citation   CrossMark

ARTICLES YOU MAY BE INTERESTED IN

Photothermal, photocarrier, and photoluminescence phenomena in semiconductors studied using spectrally resolved modulated infrared radiometry: Physics and applications
Journal of Applied Physics **126**, 150902 (2019); https://doi.org/10.1063/1.5114719

Leaky mode transition and enhanced resonance in tilted fiber Bragg grating
Journal of Applied Physics **126**, 154501 (2019); https://doi.org/10.1063/1.5121904

Electromodulation spectroscopy of highly mismatched alloys
Journal of Applied Physics **126**, 141102 (2019); https://doi.org/10.1063/1.5111965

Spatially resolved thermoreflectance techniques for thermal conductivity measurements from the nanoscale to the mesoscale EP

View Online   Export Citation   CrossMark

David H. Olson,[1] ID Jeffrey L. Braun,[1] ID and Patrick E. Hopkins[1,2,3,a)] ID

AFFILIATIONS

[1]Department of Mechanical and Aerospace Engineering, University of Virginia, Charlottesville, Virginia 22904, USA
[2]Department of Materials Science and Engineering, University of Virginia, Charlottesville, Virginia 22904, USA
[3]Department of Physics, University of Virginia, Charlottesville, Virginia 22904, USA

[a)]phopkins@virginia.edu

ABSTRACT

Thermoreflectance techniques, namely, time- and frequency-domain thermoreflectance (TDTR and FDTR, respectively), are ubiquitously used for the thermophysical characterization of thin films and bulk materials. In this perspective, we discuss several recent advancements in thermoreflectance techniques to measure the thermal conductivity of solids, with emphasis on the governing length scales and future directions in expanding these advances to different length scales and material structures. Specifically, the lateral resolution of these techniques, typically on the order of several micrometers, allows for an understanding of the spatially varying properties for various materials. Similarly, limitations of TDTR and FDTR with respect to their volumetric probing regions are discussed. With a recently developed steady-state thermoreflectance technique, these limitations are overcome as probing volumes approach spot sizes. Finally, recent pushes toward the implementation of these techniques without the use of a thin metal transducer are presented, with guidelines for future avenues in the implementation under these specimen configurations.

I. INTRODUCTION

Thermoreflectance-based techniques,[1–4] such as time- and frequency-domain thermoreflectance (TDTR[5] and FDTR,[6] respectively), have emerged as powerful thermometry platforms to measure and interrogate the thermal properties of a wide range of bulk materials and nanosystems.[7–9] For example, TDTR and/or FDTR have been used to measure the thermal conductivity of bulk solids[6,10,11] and exceptionally low thermal conductivity thin films,[12–17] volumetric heat capacity,[17–19] and thermal transport properties of nanocomposites, such as superlattices,[20–24] alloys, and nanowire matrices.[25–27] These techniques have also shown to have capabilities in the realm of interfacial conductances across material interfaces,[28] including structurally/compositionally varying interfaces,[29–36] interfaces adjacent to low dimensional structures (e.g., self-assembled monolayers and graphene),[37–41] and solid/liquid interfaces.[42–46] Iterations of these TDTR/FDTR

techniques have demonstrated the potential to go beyond measuring the thermophysical properties of systems and are capable of providing insight into the vibrational mean free path spectra of solids (i.e., relating to the "thermal conductivity accumulation function")[47–55] and the spectral coupling of phonons across interfaces (i.e., relating to the "thermal boundary conductance accumulation function").[10]

Thermoreflectance techniques, by definition, rely on the principle of thermoreflectance,[1,56–58] measuring a material's change in reflectivity due to the change in its temperature. In a typical modulated pump-probe thermoreflectance experiment such as TDTR or FDTR, a pump beam is used to thermally excite the surface of the sample at some frequency, f. The change in the intensity of a reflected probe beam is related to the temperature change on the surface as a function of either f or the delay time between the pump and probe pulses in the case of short pulsed-based experiments. Where TDTR utilizes short, typically subpicosecond, pulses to monitor the thermoreflectance decay as a function of delay time

after pump pulse heating as well as the phase shift induced from the modulated temperature change at f, FDTR can utilize a variety of pulsed or continuous wave (cw) lasers to monitor the phase shift in thermoreflectance signals solely as a function of f. When f becomes low enough, the material of interest will reach steady-state conditions during periods of the modulation event. In this regime, a third technique has recently emerged. "Steady-State Thermoreflectance" (SSTR) operates like FDTR only in the low frequency limit,[59] monitoring the thermoreflectance of the surface at increasing pump powers and inducing a Fourier-like response in the material. Ulitmately, SSTR offers an alternative method to measure the thermal conductivity of materials via optical pump-probe metrologies. The characteristic pump excitations and responses for each of these techniques are presented in Fig. 1. We review the recent advances in SSTR in Sec. IV.

In addition to their noncontact nature, these optical metrologies are advantageous relative to many other thermometry platforms in the relatively small volume and near-surface region in which they measure. By using proper laser wavelengths to ensure nanoscale optical penetration depths, the thermal penetration depth (i.e., the depth beneath the surface in which these techniques measure the thermal properties), $\delta_{thermal}$, can be limited to the focused spot size, or much less, depending on the modulation frequency. Furthermore, given that the pump and probe spot sizes can be readily focused to length scales on the order of micrometers, thermoreflectance techniques allow for spatially resolved surface measurements of thermal properties with micrometer-resolution and the ability to create thermal property areal "maps" or "images." We review the pertinent length scales of TDTR, FDTR, and SSTR in Sec. II, followed by the advances toward areal thermal property "mapping" in Sec. III.

The change in reflectivity of a given material is related to both the change in temperature of the material (i.e., the thermoreflectance, which is ultimately of interest for the measurements of temperature changes and thermal properties) and the change in the number density of the carriers excited by the optical perturbation. Thus, the total photoreflectance signal change that is measured in TDTR, FDTR, or SSTR can be expressed as the sum of these two components,[60]

$$\Delta R = \frac{\partial R}{\partial T}\Delta T + \frac{\partial R}{\partial N}\Delta N, \tag{1}$$

where $\partial R/\partial T$ is the temperature reflectance coefficient, $\partial R/\partial N$ is the free-carrier reflectance coefficient, and ΔT and ΔN are the changes in temperature and free carriers from the pump excitation, respectively. In the majority of thermoreflectance measurements reported in the literature, samples of interest are coated with a thin metal film transducer, in which the change in reflectivity is directly related to the change in temperature. This comes with the advantage that the optical penetration depth in metals is confined to <20 nm over a wide range of optical wavelengths, resulting in a "near-surface" heating event. An additional advantage of using a metal film transducer is that the $\frac{\partial R}{\partial N}\Delta N$ term in Eq. (1) is much smaller than $\frac{\partial R}{\partial T}\Delta T$, except for when pump excitations induce interband transitions and their contributions become comparable. Even so, the contribution to ΔR from $\frac{\partial R}{\partial N}\Delta N$ lasts only for ~1 ps for most metals.[61,62] This is unlike nonmetals where not only temperature, but also conduction band carrier population can change the reflectivity significantly for lifetimes much longer than a picosecond.[63–65] However, if the optical and thermal penetration depths of the pump and probe beams are properly accounted for,
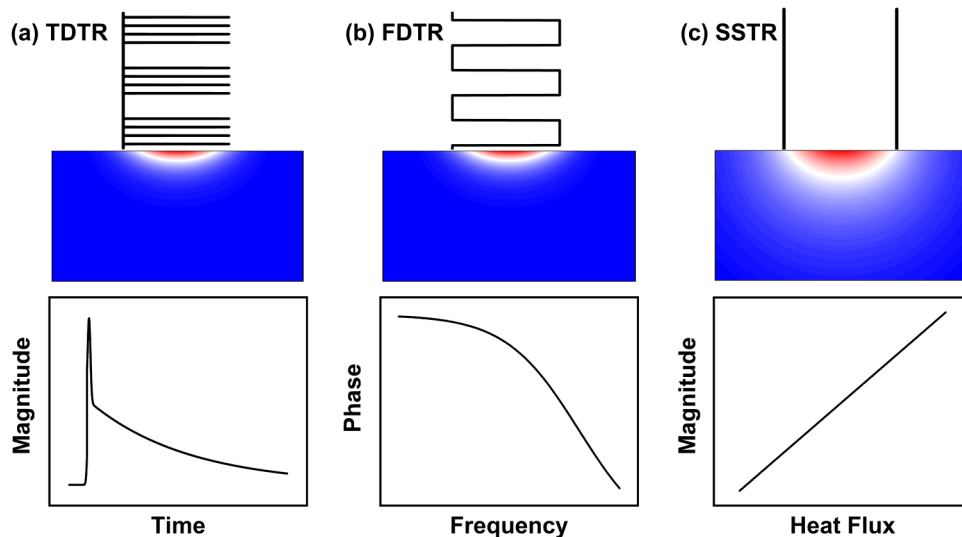
FIG. 1. Characteristic excitations and corresponding responses for (a) TDTR, (b) FDTR, and (c) SSTR techniques. In TDTR, the magnitude of the thermoreflectance is monitored as a function of pump-probe delay time, while in FDTR, the thermally-induced phase lag between the pump and probe is monitored as a function of frequency. In SSTR, the steady-state induced magnitude of the thermoreflectance is monitored for given changes in heat flux. Notice the increase in thermal penetration depth, $\delta_{thermal}$, in SSTR resulting from the lower modulation frequencies employed as compared to TDTR and FDTR.

and the thermoreflectance signal in the measured photoreflectance response can be isolated from the free-carrier response (i.e., if the first term on the right hand side in Eq. (1) can be separated from the second term on the right hand side), then TDTR, FDTR, and SSTR can be conducted without the use of a metal film transducer, giving rise to increased measurement sensitivities to different thermal properties of materials that are not necessarily accessible in the traditional metal-transducer configuration. We review recent advances in TDTR and FDTR without a metal film transducer and provide guidelines for the implementation in SSTR in Sec. V.

The remainder of this perspective is structured as follows. Section II will discuss the pertinent length scales associated with thermoreflectance techniques, with emphasis on the thermal penetration depth, and, therefore, the probing volume, in these experiments. Section III will discuss the lateral resolution associated with these techniques, abstracting them to a spatial understanding of variations in thermoreflectance and, therefore, thermal properties. Section IV will review the newly-developed SSTR technique, offering future avenues of exploration. Finally, Sec. V extrapolates the use of these techniques to their implementation without the use of a thin metal transducer. Section VI will provide a final perspective and offer guidelines for each of these implementations in the future.

II. THERMOREFLECTANCE LENGTH SCALES

The length scales associated with thermoreflectance techniques make them applicable to a wide range of material systems and geometries. Because pump and probe beams are typically collinearly aligned through objective lenses with high numerical apertures, lateral resolution in these measurements can be on the order of micrometers. The through-plane resolution is often described by the thermal penetration depth, δ_{thermal}, mathematically defined as the depth at which the temperature decays to $1/e$ of its value on the heated surface as a result of a modulated heating event. This depth is typically considered the probing depth under the surface in modulated thermoreflectance experiments. The subsurface temperature distribution of a semi-infinite medium follows the iterative algorithm as proposed by Carslaw and Jaeger,[66]

$$T(z) \sim e^{-qz}. \tag{2}$$

In this equation, q is the complex wavevector, defined by $\sqrt{k^2 + \frac{i\omega}{D}}$ for isotropic media, where ω is the angular frequency of the heating event, D is the thermal diffusivity, and k is the Hankel transform variable over which the integration is performed to extract the surface temperature.[67] Without a loss of generality, $k \sim w_{01}^{-1}$, where w_{01} is the effective pump/probe $1/e^2$ radius, and is a value that is consistent with the upper bounds of integration to extract the surface temperature. In the high frequency limit, $\omega \gg D/w_{01}^2$,

$$\delta_{\text{thermal}} = \sqrt{\frac{2D}{\omega}}, \tag{3}$$

and is the definition most commonly used for the penetration depth associated with pump/probe thermoreflectance experiments. Various works have relied upon Eq. (3) in their analysis of thermal conductivity accumulation and mean free paths in TDTR
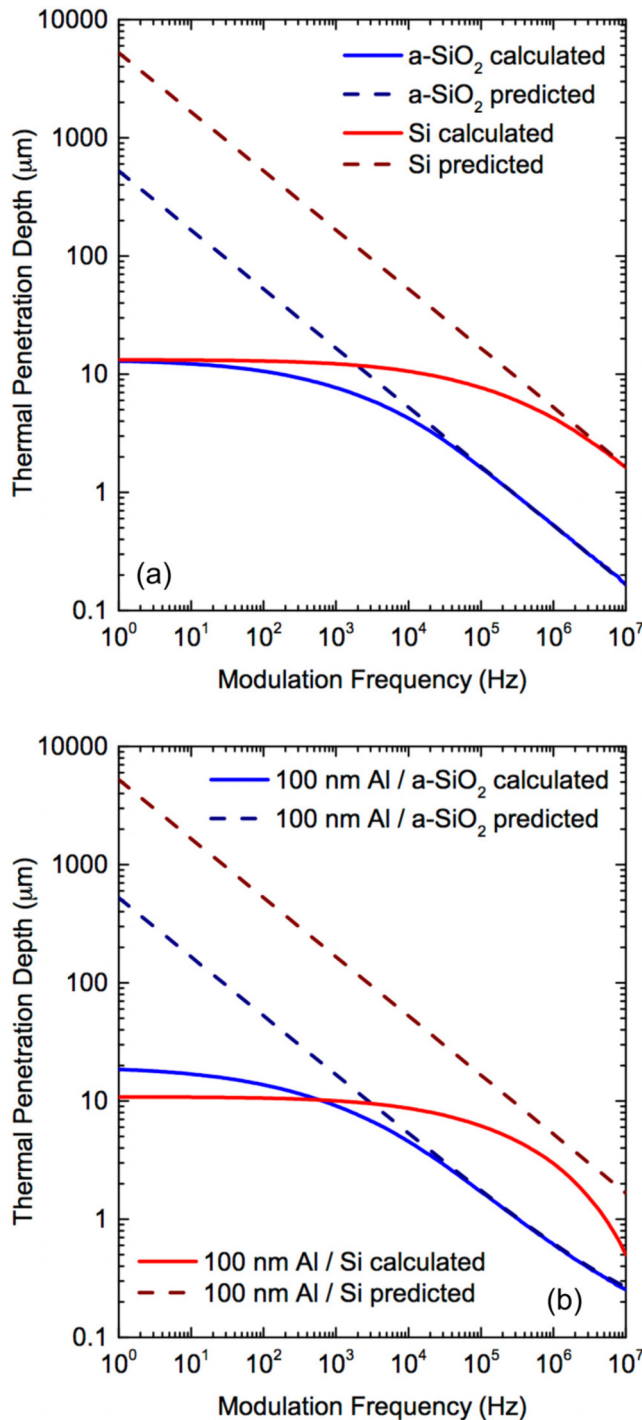
and FDTR studies.[49,68,69] In the low frequency limit, $\omega \ll D/w_{01}^2$, however,

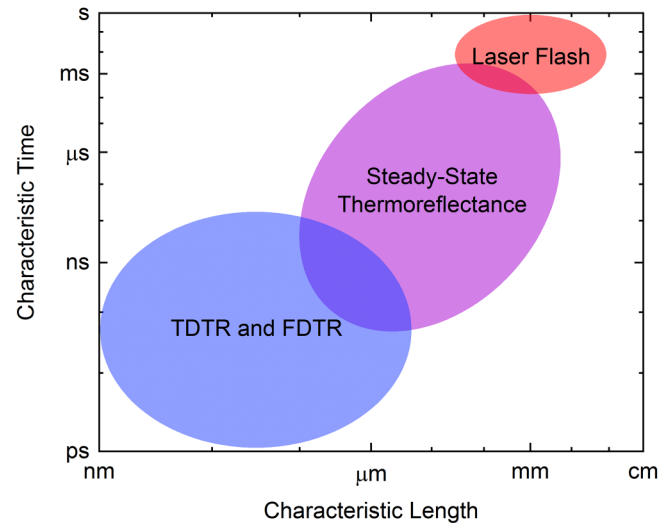$$\delta_{\text{thermal}} = w_{01}, \tag{4}$$

which fundamentally limits the penetration depth of pump/probe experiments to the heater radius for the case of a semi-infinite medium. In material systems consisting of two layers or more, Eqs. (3) and (4) fail to adequately describe δ_{thermal}, as both interfacial resistances and heat spreading have the potential to strongly influence this descriptor.[70]

As an example, we present the associated thermal penetration depths for a-SiO$_2$ and Si coated with and without an Al transducer in Fig. 2, calculated from the numerical solution to the cylindrical heat equation from Braun and Hopkins.[70] In the high frequency limit, ≥ 1 MHz, good agreement is found between Eq. (3) and the numerical results for the bulk uncoated a-SiO$_2$ and Si, validating δ_{thermal} in the high frequency limit. Nonetheless, there are inherent limitations in assuming Eq. (3) for all frequencies of modulation, especially when considering samples coated with metal film transducers. As $f \to 0$, δ_{thermal} calculated via Eq. (3) approaches infinity, suggesting that depths much larger than the pump/probe radii can be probed. Not only is this unphysical, it is also thwarted by the complex multilayer systems typically analyzed using TDTR and FDTR. In the low frequency limit, the thermal penetration depth is limited by the effective $1/e^2$ pump/probe radius, exemplified by Eq. (4) as well as in Fig. 2(a) for a-SiO$_2$ and Si without a metal transducer.

The inclusion of a thin metal transducer also has significant implications on δ_{thermal}. This stems from both the in-plane heat spreading in the metal film as well as the associated resistance at the metal/substrate interface. On a thermally insulating substrate, for example, the temperature gradient will be preferentially formed laterally in the metal film before entering into the substrate and decaying as normal. This is shown in Fig. 2(b) for a-SiO$_2$ coated with 100 nm Al. Compared to the direct heating of a-SiO$_2$, the $1/e$ thermal penetration depth in the low frequency limit is increased as a result of heat spreading in the Al and thus an increase in the effective heater radius. The interfacial resistance at the metal/substrate interfaces begins to play a significant role when the resistance of the metal/substrate interface is comparable to the resistance of the volume probed in the substrate, i.e., $R_{\text{thermal}} \sim \delta_{\text{thermal}}/\kappa$, where R_{thermal} is the resistance of the metal/substrate interface and κ is the thermal conductivity of the substrate. If we assume that $R_{\text{thermal}} = 10 \text{ m}^2 \text{ K GW}^{-1}$ for Al/a-SiO$_2$ and Al/Si, for example, the associated penetration depths required for the resistances of the two systems to be equivalent are ~ 15 and ~ 1500 nm for a-SiO$_2$ and Si, respectively. This is most impactful for Si, shown in Fig. 2(b). In the low frequency limit, a reduction in the $1/e$ penetration depth occurs as a result of this criteria, as the associated temperature drop at the interface is on the order of or greater than that in the Si. In the high frequency limit, the deviation between Eq. (3) and the numerical solution begins at ~ 1 MHz, associated with a penetration depth of ~ 1 μm, for similar reasons. One would expect similar deviations at modulation frequencies approaching the GHz range for a-SiO$_2$. The above discussions regarding the associated probing depths at the low frequency limit have provided a fundamental foundation for SSTR,

FIG. 3. Characteristic length and time scales associated with laser-based techniques used to extract thermophysical properties.

FIG. 2. Thermal penetration depth for (a) bare and (b) 100 nm Al coated a-SiO$_2$ and Si. The solid lines are determined numerically in the work of Braun and Hopkins,[70] while the dashed lines are calculated from Eq. (3). Reprinted with permission from Braun and Hopkins, J. Appl. Phys. **121**, 175107 (2017). Copyright 2017 AIP Publishing LLC.

which inherently relies on the steady-state temperature rise of a material system as a result of the low frequencies of heating, where the penetration depth is on the order of the spot size.

As a result, a new regime previously untapped regarding measurement length scales has been uncovered. Summarized in Fig. 3 are conventional optical metrologies used for the extraction of thermophysical properties and their associated characteristic length and time scales. In time- and frequency-domain thermoreflectance techniques, the high frequencies of modulation inherently limit the probing volume on the order of 100s of nanometers to 1 μm for most materials. On the other hand, sample size restrictions via the laser flash technique are typically limited to $\geq 100\,\mu$m.[71] SSTR offers a novel regime of measurement length scales, as spot sizes can be tuned between several micrometers and millimeters, power permitting. SSTR is further discussed in Sec. IV.

III. SPATIALLY MAPPING THERMAL CONDUCTIVITY WITH MICROMETER-SCALE RESOLUTION

The ability to locally probe regions of interest with these thermoreflectance techniques makes high spatial resolution mapping a logical extension. With lateral resolution on the order of the spot size, the techniques naturally lend themselves to observe local variations in thermoreflectance, and, therefore, local variations in thermal properties. While full-field thermoreflectance techniques offer immense capabilities in terms of reaching diffraction-limited resolution and monitoring localized variations in temperature,[72,73] they are generally unable to extract the associated varying thermal properties for complex, layered material systems. In Subsections III A and III B, we outline the implementation of thermoreflectance mapping via TDTR and FDTR, elucidating key differences between the two techniques and highlighting a multitude of relevant scenarios in which micrometer-scale thermal

property mapping shows good applicability for understanding the underlying thermal physics.

A. Introduction and implementation

Spatial monitoring of the thermoreflectance of material systems was first implemented in the early 1980s.[74,75] An example of a spatially resolved thermoreflectance line scan is shown in Fig. 4 for a patterned $^{75}As^+$ implanted Si wafer. The small spot sizes of the pump/probe laser beams ($\sim 1\,\mu m$) allow for monitoring the pattern with high spatial resolution and throughput. Similar techniques monitoring the associated thermoreflectance were presented in a variety of following works.[76–84] Quantification of the associated thermal properties of given material systems, however, has only recently been developed due to a broader understanding of the associated analysis with thermoreflectance techniques,[5,67,85] including the inclusion of a metal transducer to enhance sensitivity to underlying material properties and incite a near-surface heating event due to the shallow optical skin depth.[86]

1. Time-domain thermoreflectance

In TDTR, thermal properties are extracted from the radially symmetric heat diffusion during a pulsed heating event.[5] While readily implemented, performing full TDTR scans (time delays from 0 to $\sim$5 ns, which corresponds to 2–3 minutes per scan) across the surface of an entire sample to create these spatially resolved thermal property maps can thus be time consuming. To overcome this limitation, two experimental variables can be manipulated and judiciously chosen to enhance sensitivity to the
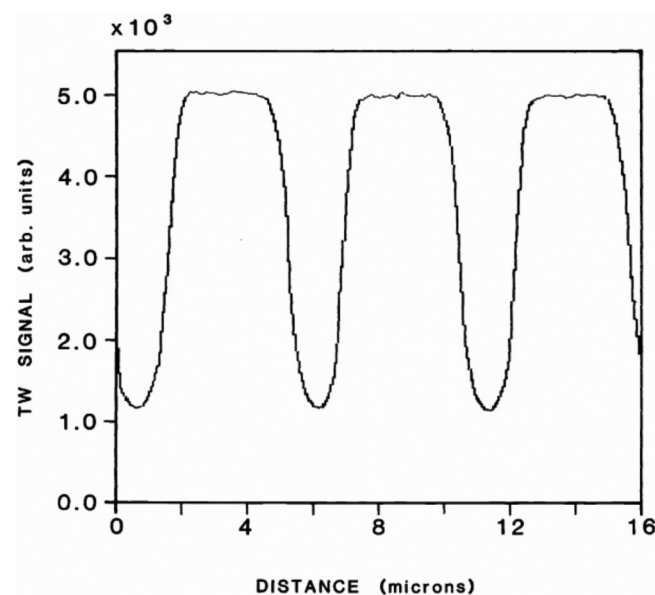

FIG. 4. Thermal-wave (TW) line scan of a patterned Si sample implanted with $^{75}As^+$ at 125 keV. Reproduced with permission from Smith *et al.*, Proc. SPIE **0530**, 201–214 (1985). Copyright 1985 SPIE.

parameter of interest: (1) the modulation f and (2) the pump-probe delay time. In doing so, high-throughput raster scans over a given region of the sample can be performed. Huxtable *et al.*[87] first presented this thermal conductivity mapping procedure for TDTR in an effort to better describe a combinatorial Nb–Ti–Cr–Si system. Full TDTR scans from their work are shown in Fig. 5(a) for regions composed primarily of Cr, Nb, and Ti. At intermediate delay times, $50 \leq t \leq 300$ ps, the ratio $-V_{in}/V_{out}$ approximately scales with the thermal effusivity, $\sqrt{\kappa C}$. For material systems in which there are large variations in effusivity, these intermediate pump-probe delay times are ideal, and the thermal conductivity of a particular region can then be extracted with knowledge of its volumetric heat capacity. Additionally, at these delay times, sensitivity to the thermal boundary conductance at the metal transducer/substrate interface is relatively low. This is best exemplified by the thermal conductivity correlation curve, shown in Fig. 5(b) for the combinatorial Nb-Ti-Cr-Si system in Ref. 87. The upper and lower bounds of G suggest that small variations in G do not significantly impact the thermoreflectance signal and, therefore, the extracted thermal conductivity. The final thermal conductivity micrograph of the system can be seen in Fig. 5(c).

An alternative approach to this intermediate pump-probe delay time is appropriate when the material system of interest does not show large variations in volumetric heat capacity; this can be specific to single-phase systems or systems of varying crystalline orientation. In this scenario, knowledge of the interfacial conductance allows for the minimization of its sensitivity such that variations in G result in minute alterations in the extracted thermal conductivity. The general process includes the extraction of G and its uncertainty from a variety of full TDTR measurements. Next, a sensitivity analysis is performed, and the delay time at which the sensitivity to G is minimized is chosen as the delay time for the mapping procedure. This analysis becomes difficult when the thermal conductivity of the underlying material is low, and the sensitivity to G does not go to zero for the given delay times. This can be overcome by reverting to the previous option, whereby the delay time is fixed to short, intermediate delay times, or by implementing an FDTR-like approach to extract G and κ simultaneously via a multimodulation frequency approach, as discussed below. Multiple maps can also be performed with alterations in modulation frequency and delay time to extract additional parameters. Alternatively, the implementation of a heterodyne picosecond thermoreflectance (HPTR) technique would prove to be advantageous, as simultaneously fitting multiple parameters would be possible with a single acquisition by tracing the entire thermoreflectance decay at each pixel.[88,89]

2. Frequency-domain thermoreflectance

In FDTR, the radially symmetric heat diffusion equation is compared to a pulsed-pulsed or cw-cw frequency sweep to extract parameters of interest. If the lock-in amplifier is permitting, a multimodulation frequency approach can be used to extract multiple parameters simultaneously. This was first exemplified in the work of Yang *et al.*[90] using an FDTR configuration, whereby the pump was modulated at 6 independent frequencies to extract both the interfacial conductance and substrate thermal
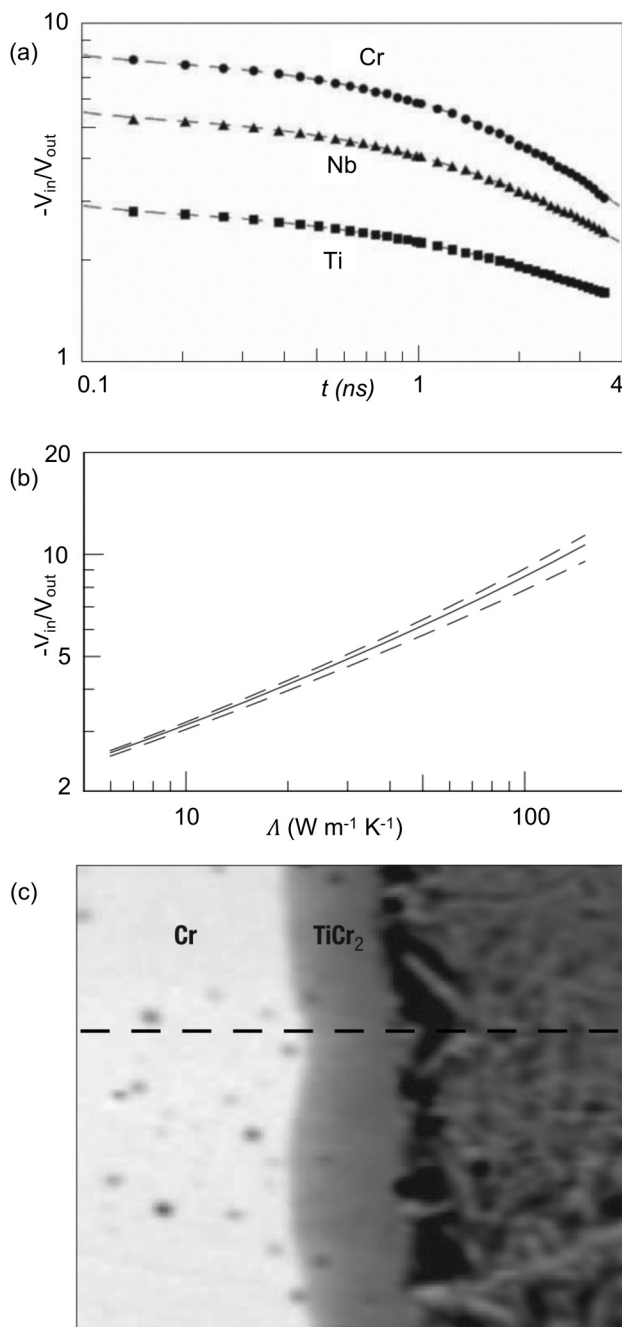
FIG. 5. (a) TDTR data and models for Cr, Nb, and Ti regions on a Nb–Ti–Cr–Si diffusion multiple. (b) Correlation function of the substrate thermal conductivity to ratio $-V_{in}/V_{out}$ used to extract the thermal conductivity during the mapping procedure. The solid line is for $G = 140 \, \text{MW m}^{-2} \, \text{K}^{-1}$, while the upper and low dashed lines are for $G = 200$ and $100 \, \text{MW m}^{-2} \, \text{K}^{-1}$, respectively. (c) Thermal conductivity micrograph of the combinatorial system. The scale is logarithmic such that black and white regions are 6 and $120 \, \text{W m}^{-1} \, \text{K}^{-1}$, respectively. Reprinted with permission from Huxtable et al., Nat. Mater. **3**, 298–301 (2004). Copyright 2004 Springer.

conductivity, G and κ, respectively, of Si patterned with Au/Ti contacts, summarized in Fig. 6. Figures 6(a) and 6(b) show the FDTR data and best fit and sensitivity to G and κ, while Fig. 6(c) shows the phase micrographs at the 6 frequencies. Little contrast can be seen in the phase micrographs at 37.9, 431.7, and 901.3 kHz, consistent with the low sensitivity to G at these
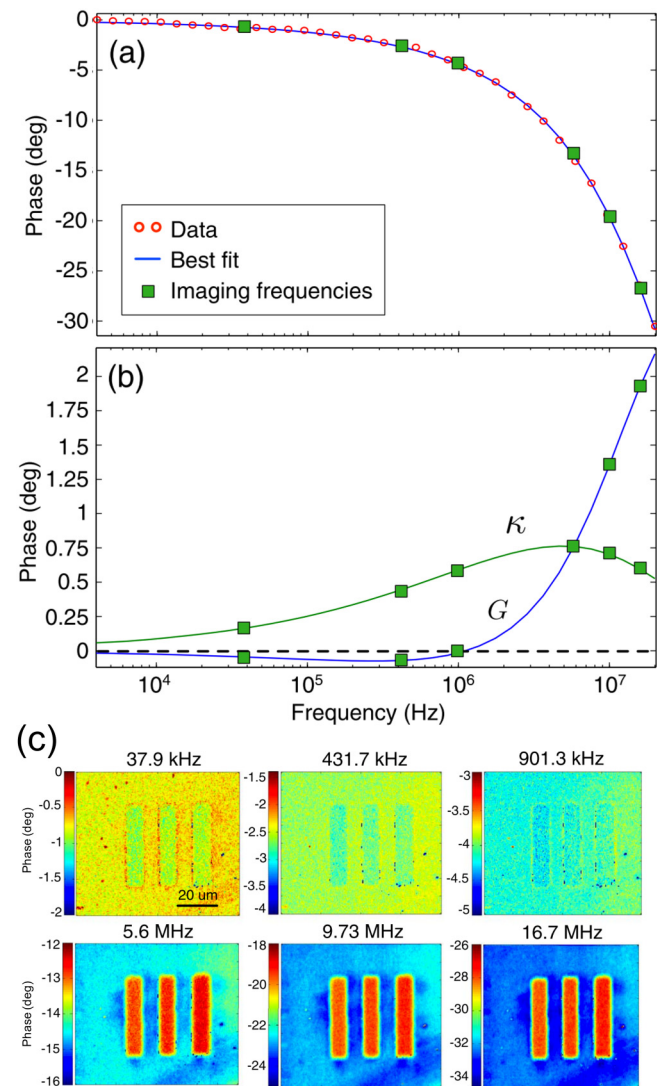
FIG. 6. FDTR implementation of a thermal conductivity mapping procedure of Si patterned with Au/Ti contacts. Data and best fit from a full FDTR scan are presented in (a), while the sensitivity to the the interfacial conductance and substrate thermal conductivity G and κ, respectively are shown in (b). Imaging frequencies are also identified at 37.9 kHz, 431.7 kHz, 901.3 kHz, 5.6 MHz, 9.73 MHz, and 16.7 MHz. Note that a frequency is chosen when sensitivity to G is near zero. Phase images at the six frequencies are shown in (c). Notice the lack of contrast at 901.3 kHz, where sensitivity to G is near zero. Reprinted with permission from Yang et al., Rev. Sci. Instrum. **84**, 104904 (2013). Copyright 2013 AIP Publishing LLC.

modulation frequencies. Contrarily, at 5.6, 9.73, and 16.7 MHz, the large sensitivities to G result in large contrasts in the associated phase micrographs. Thus, at 6 independent frequencies, the sensitivity to G and κ is fully captured and allows for a robust characterization of the material system. Using a similar mapping procedure, Hatori et al.[91] have shown that a single modulation frequency can be used to extract the thermal effusivity in a fiber composite material, suggesting that modulating the pump at multiple frequencies is not necessary.

3. Implementation

The implementation of a thermoreflectance mapping technique, be it TDTR- or FDTR-based, requires interfacing between components of the imaging system, most importantly the motorized stage for sample positioning and lock-in amplifier, to allow for a high-throughput imaging technique. Because alterations in the alignment of either of the aforementioned systems is not ideal, samples are typically rastered with respect to the pump and probe beams rather than relying on galvomirrors that would alter the detection aspect of these methods. The method of rastering is dependent on the user and the available components. This can stem from a stepperlike action or a method that scans continuously. Both require careful choices of the lock-in amplifier acquisition parameters, with knowledge of the scan velocity in the latter case. We emphasize that the spot size must be continuously in focus to extract an appropriate thermoreflectance signal in both of these cases. Focal changes on the order of the spot radius have a quantifiable impact on the effective pump/probe size and, therefore, the extracted parameter of interest. Since spot sizes approaching ∼1 μm become the most sensitive parameter in these thermoreflectance techniques,[6,92] defocusing of the pump and probe spots can and should be remediated. Here are possible mitigation strategies to avoid this source of uncertainty, if present:

1. If the size of the spot is large, or if the spot does not change focus over the duration of the map, then a focus at the beginning of the mapping procedure should suffice. The user should ensure, however, that no focal changes are taking place with a reference sample or by some other means.
2. An autofocus procedure can be performed at each pixel, by maximizing the magnitude of the thermoreflectance signal or through some other quantifiable means. While simple, the procedure is time consuming, as the autofocus procedure may take on the order of several seconds to complete. This adds unwanted waiting time in the mapping procedure and greatly increases the overall acquisition time.
3. An autofocusing procedure can be performed at the beginning of the image in the center of the map. This ensures that the majority of the map, depending on its dimensions, is in focus. Depending on the orientation of the sample and the motorized stage, this usually results in a defocused spot size toward the edges of the map and, therefore, erroneous thermoreflectance signals in these regions that do not adequately describe the specimen of interest.
4. An autofocusing procedure that is performed at the corners of the image prior to the acquisition. This allows for the user to extract the "plane" of focus, allowing for adjustments to be

made during the mapping procedure. This ensures that the beam is in focus for the entirety of the map and is far more ideal as compared to options (2) and (3).

Care should be taken to monitor any potential changes in the environment and electronics when a mapping procedure is being performed. This includes, but is not limited to, changes in local temperature gradients, which can alter the focus of the sample, drift of power for the pump and probe laser, changes in the pump phase, and diffusely scattered light caused by surface inhomogeneities at the sample surface. The last of these can be overcome by monitoring the DC reflected probe signal, as diffuse scattering will result in a reduced DC signal, and highlighting regions in which the data are not to be analyzed.

In Subsection III B, we show how thermoreflectance mapping can be applied to a variety of relevant material systems.

B. Applicability to material systems

Thermal property microscopy has applications in a variety of material systems. It is particularly applicable in systems in which changes in composition, layering, homogeneity, etc., are present. Here, we highlight a number of works that utilize a mapping procedure to extract a variety of properties of interest. First, the mapping procedure is employed in combinatorial material systems, whereby multiple phases of materials are present to extract their thermal properties of interest. Furthermore, the application toward thermal barrier coating systems consisting of various coatings is shown. In more recent works, the procedure has been pushed toward the characterization of high thermal conductivity and 2D materials to provide a better understanding of the underlying phonon physics.

1. Combinatorial materials

Combinatorial materials present a unique opportunity to extract thermal properties of novel materials and phases and the variation of these thermal properties around heterogeneous material interfaces. With robust deposition and characterization techniques, the fabrication of these material systems has become increasingly rapid and reliable. Here, we highlight works that examine the combinatorial thermal nature of Nb–Ti–Cr–Si (Ref. 87) and Cr–Pd–Pt–Rh–Ru (Refs. 93 and 94) diffusion multiples via a TDTR mapping approach. d'Acremont et al. have also shown the ability for HPTR to characterize a ternary thin film silicide library.[89]

A summary of the results for the Nb–Ti–Cr–Si diffusion multiple are shown in Fig. 5. The delay time was set to 92 ps to extract the normalized effusivity of the material system. Specifically, the extraction of the Laves phase of $TiCr_2$ of varying Cr stoichiometry was extracted. For a Ti content increase from 33.5 at. % to 36.1 at. %, there is a corresponding decrease in the thermal conductivity from 42 to 20 W m^{-1} K^{-1}. Additionally, the b.c.c. phase of a Ti alloy (85.5 at. %) with Cr (14.5 at. %) is extracted, yielding a thermal conductivity of 7.5 W m^{-1} K^{-1}. The thermal conductivity mapping procedure creates a visual representation of the thermal conductivity variations in this Ti/Cr system and a much higher throughput than standard TDTR. Especially for the Laves phases of $TiCr_2$, nearly 20 points comprise the region from 33.5 at. % Ti to 36.1 at. %. With an acquisition time of ∼3 s per pixel, this takes

approximately 60 s. Contrarily, performing full TDTR scans in each of the 20 regions would have resulted in 40 min of acquisition time, assuming 2 min for a given scan. An additional avenue of interest is presented at the triple junction of Nb–Si–Ti in this same work.[87] Specifically, grains of the (Ti,Nb)$_3$Si phase are present with differing thermal conductivities. The differences in observed thermal conductivity are attributed to differing orientations, suggesting the ability to extract the thermal conductivity tensor of a material system via thermal conductivity mapping.

Using combinatorial material systems has the advantage of creating multiple phases on a single sample. This allows for the robust characterization of various alloys that would otherwise be fabricated on numerous separate samples, adding the potential for additional complexities, uncertainties, and time for complete characterization. Nickel-based super alloys are typically used in high temperature applications in a wide range of compositions. In fabricating Cr–Pd–Pt–Rh–Ru diffusion multiples, Zheng *et al.*[94] were able to examine the electronic contribution to thermal conductivity in a wide range of Ni alloys, where ~50 Ni(Cu,Fe) alloys had been measured on a single wafer. In fabricating the diffusion multiple, 125 data points over a 250 μm length were taken with relative ease. At 3 points per second,[94] this measurement procedure takes about 6 min. We reiterate the fact that using conventional TDTR performed at each of these data points would have taken an order of magnitude longer in acquisition time. Ultimately, the fabrication of this diffusion multiple allowed for the robust and high-throughput validation of the Wiedemann-Franz law in Ni alloys over a wide range of compositions.

2. Coatings

Coatings are an integral component in a variety of research applications, whereby the coating enables some level of environmental or thermal protection, or some additional functionality, enhancing the performance of the underlying media. For example, thermal barrier coatings in aerospace applications preferably have a low thermal conductivity to protect the underlying turbine blade, allowing for an increase in gas engine operating temperatures and efficiency.[97] On the other hand, in nuclear power generation contingent on UO$_2$ kernels, the efficiency is dictated by heat transfer into the coolant from the fuel particle,[98,99] and thus, a high thermal conductivity is preferable so as to not induce large temperature gradients.

Work in the literature is sparse regarding the thermal conductivity mapping of thermal barrier coatings. However, considering the possibly multiphase, anisotropic materials that constitute these coatings from various application processes, more research in this field is deserving. To date, few works have rigorously examined the spatial profile of thermal conductivity in barrier coating components. Figure 7 shows an example of a yttria-stabilized zirconia (YSZ) thermal barrier coating system on a two-phase Nb silicide composite substrate bonded by a multiphase bond coat.[100] As is evident, the thermal conductivity of the YSZ is low as compared to the Nb silicide composite, which is preferable in this system. While contrasts in the thermal conductivity of this specific YSZ barrier coating are not large, the procedure presents itself to a wide variety of applications in the barrier coating community. This can include structural influences on the thermal conductivity of the barrier
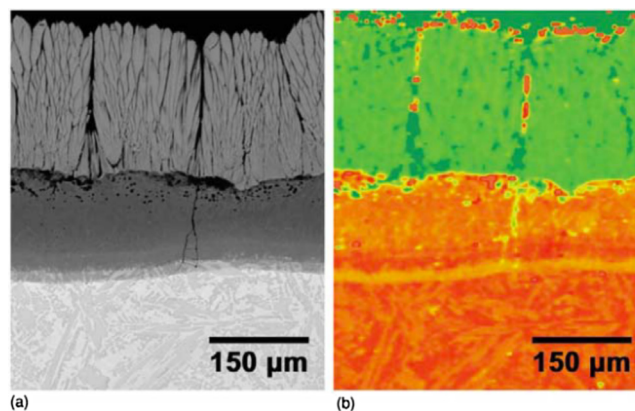

FIG. 7. (a) Backscattered electron and (b) thermal conductivity micrograph of a yttria-stabilized zirconia (YSZ) thermal barrier coating (TBC), bond coat, and Ni superalloy substrate system. Reprinted with permission from Zhao *et al.*, Mater. Today **8**, 28–37 (2005). Copyright 2005 Elsevier.

coating itself or understanding the effect of cycling on other components, such as the thermally grown oxide that is necessary for the fabrication of these systems. Similar implementations of such a mapping procedure have also been performed on pyrolytic carbon and silicon carbide coatings for UO$_2$.[101]

3. Two-dimensional materials

Two-dimensional and quasi-two-dimensional materials present themselves with a wide range of applications including supercapacitors and batteries,[102] THz emitters/detectors,[103] and field effect transistors,[104] to name a few. Beyond their intrinsic properties, this is in large part due to the vast capabilities of introducing dopants so as to exude properties of interest.[104–107] Because of their two-dimensional nature, measurements of the thermal properties become increasingly difficult due to the time constant associated with heat transport in these materials.[108] Nonetheless, various works have examined thermal transport in and through relevant material systems with success, both with thermoreflectance techniques and other techniques.[109–112] In thermoreflectance techniques, this has been primarily limited to extracting conductances at interfaces with these materials. This is due to the general lack of sensitivity to cross- and in-plane transport in 2D materials via these techniques. The spatial implementation of these techniques is less common throughout the literature but still provides important insights in various material systems.

Yang *et al.*[40] presented a work focusing on the examination of in-plane conductances in few-layer graphene and implements a spatial mapping procedure with FDTR to extract a distribution of the basal-plane thermal conductivity of few-layer graphene. This was achieved by implementing a multimodulation frequency approach to capture all potential sensitivity to both the cross- and in-plane conductance in these layers. At their spot sizes (~1 μm effective pump/probe radii), in-plane heat spreading due to the Au has a more pronounced effect, and thus, its thermal conductivity must be rigorously determined. An example of the final result is
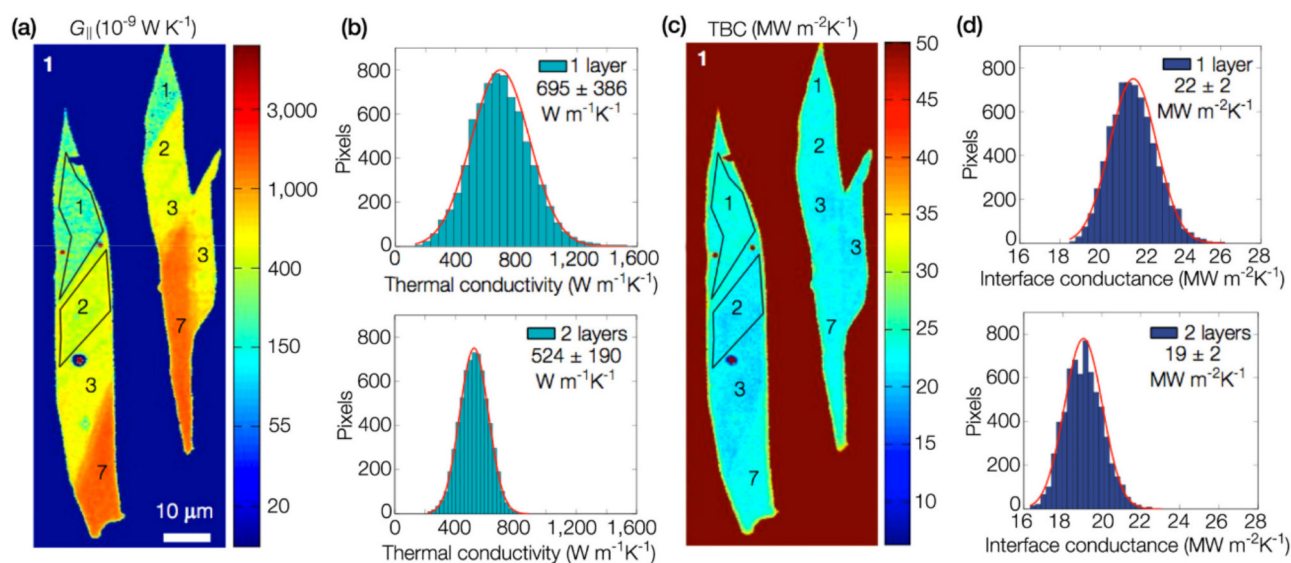
FIG. 8. Conductance micrographs for the (a) in-plane and (c) cross-plane conductances of few-layer graphene. Distributions for the in-plane thermal conductivity of mono- and bilayer graphene as extracted from their respective in-plane conductances are shown in (b), while those for the cross-plane conductance are shown in (d). Reprinted with permission from Yang et al., J. Appl. Phys. **116**, 023515 (2014). Copyright 2014 AIP Publishing LLC.

presented in Fig. 8, which shows the in-plane conductance of a graphene flake of several layers alongside the basal-plane thermal conductivities of 1- and 2-layer graphene. The large uncertainties associated with the extracted values can be attributed to the minute changes in the phase resulting from the contribution to in-plane heat spreading from the graphene layer as compared to the Au transducer. The cross-plane thermal boundary conductance, on the other hand, can be extracted more easily.

Several other works have examined the conductance at 2D material interfaces and contacts using TDTR.[113,114] However, at a single pump-probe delay time and modulation frequency, it is difficult to adequately extract parameters of interest in these systems, namely, the conductance at these contacts. The majority of works report on 2D materials on a thermally grown oxide. Thus, the sensitivity to the conductance is greatly subdued due to the low thermal conductivity of the thermal SiO_2. This has shown to impact the results of Brown et al.[114] on $MoSe_2$, whereby there is a disparity between the mapped conductance and the conductance extracted via a standard TDTR measurement. While the trends were comparable, the absolute values differed quite significantly and can be attributed to overall lack of sensitivity to the conductance for a single delay time and single modulation frequency. Ideally, this can be remediated by a multimodulation frequency approach and fitting to a model in the frequency domain.

4. Thermal management

The management of heat from a dynamic and static perspective is a consideration that must be taken into account for a variety of applications. From a static perspective, heat sinks typically have a large thermal conductivity to better manage large temperature

rises in devices.[115] Thus, materials such as diamond,[116] SiC,[117] BAs,[118–120] to name a few, are all at the forefront of thermal management from a static point of view. Dynamic thermal management additionally has a variety of applications. These range from thermally driven logic,[121] thermoelectric efficiency enhancement,[122–124] and improved heat sinking for device cooling,[125,126] but the implementation is much more difficult than dynamic electrical management. Spatially resolved thermoreflectance techniques have good applicability in understanding materials that are used in thermal management from both a static and dynamic perspective.

An important consideration in the fabrication of devices from a thermal perspective is the inclusion of grain boundaries, which have the potential to significantly impact the thermal conductivity of a material system.[127,128] When the phonon mean free paths in a material are on the order of, or greater than, the measurement spot size, these length scales can now be probed via thermoreflectance mapping techniques, which will provide a more robust understanding of the physics surrounding grain boundary scattering. This was exemplified in polycrystalline diamond, whereby a reduced thermal conductivity was observed within 10 μm of an individual grain boundary.[95] A better visualization of this is presented in Fig. 9, which shows electron-backscatter diffraction and thermal conductivity maps of a diamond polycrystal. Also included in the figure is the analysis showing a reduction in thermal conductivity as the measurement approaches the grain boundary.

Thermoreflectance imaging has also been implemented in the lithiation and delithation processes of single crystal 2D layered MoS_2.[96] In these processes, the electrochemical intercalation of Li ions is induced and reversed by the application of a voltage. The distribution of Li ions for a given MoS_2 crystal is not uniform[129,130] and thus naturally lends itself as an opportunity for thermoreflectance
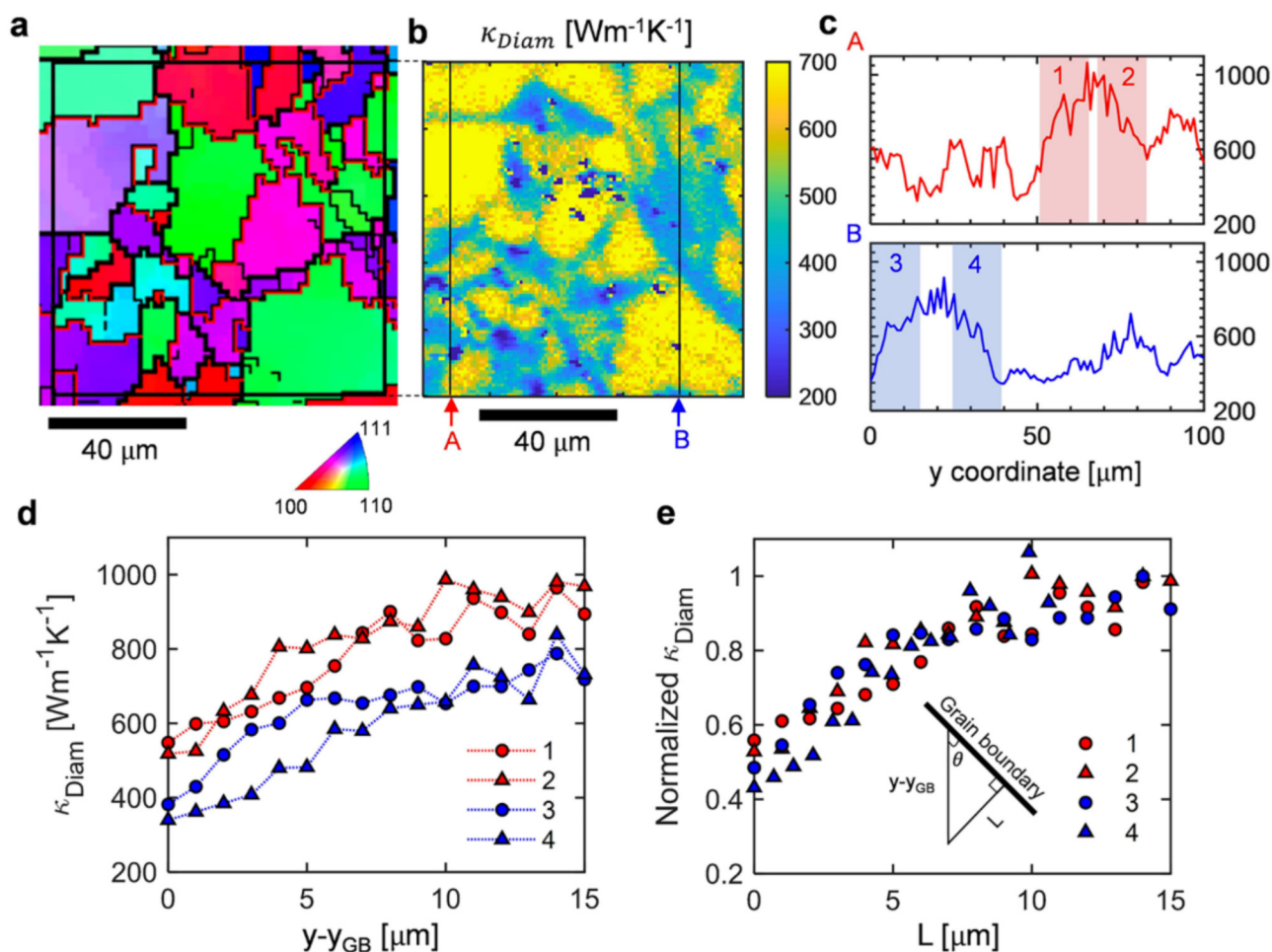
FIG. 9. (a) Electron-backscatter diffraction and (b) thermal conductivity micrographs of a polycrystalline diamond sample. (c) Line scans extracted from (b) showing the variation in thermal conductivity near grain boundaries. Included are regions near grain boundaries marked 1–4. (d) Extracted thermal conductivity relative to the position of the grain boundary. (e) Normalized thermal conductivity relative to the position of the nearest grain boundary, L. The inset shows the calculation of L; θ denotes the orientation of the grain boundary with respect to the micrographs in (a) and (b). For grain boundaries 1–3, $\theta \sim 90$, while for grain boundary 4, $\theta \sim 45$. Reprinted with permission from Sood *et al.*, Nano Lett. **18**(6), 3466–3472 (2018). Copyright 2018 American Chemical Society.

mapping. Shown in Fig. 10 are micrographs during lithiation and delithiation processes of a ~10 nm MoS_2 flake via TDTR. Evidently, the thermal conductance is varied drastically as a result of the lithiation/delithiation process, with an order of magnitude change in conductance. Furthermore, while traditional TDTR can successfully track the intercalation process, spatially understanding the inhomogeneity of the process allows for an understanding of hot spot generation in devices contingent on the intercalation process.

C. Summary and future directions for spatially-resolved thermal conductivity measurements with thermoreflectance

In this section, we have presented the basis of a thermoreflectance mapping procedure in TDTR and FDTR configurations.

The ability to monitor the thermoreflectance spatially allows for high-throughput acquisition capabilities of the thermal properties of interest. Specimens in which there are large surface inhomogeneities due to compositional variations, localized grain orientations, or when extrinsic influences impact the observed thermal conductivity are ideal for these kinds of mapping procedures. We provided several examples, including diffusion multiples, barrier coating materials, and 2D materials. Thermoreflectance mapping with micrometer-scale areal resolution has large implications for the high-throughput extraction of the thermal properties of these materials and can be readily implemented with the addition of standardized stages.

Despite these significant advances in using thermoreflectance techniques to spatially resolve variations in thermal conductivity, there are several future avenues that can be taken. We have already
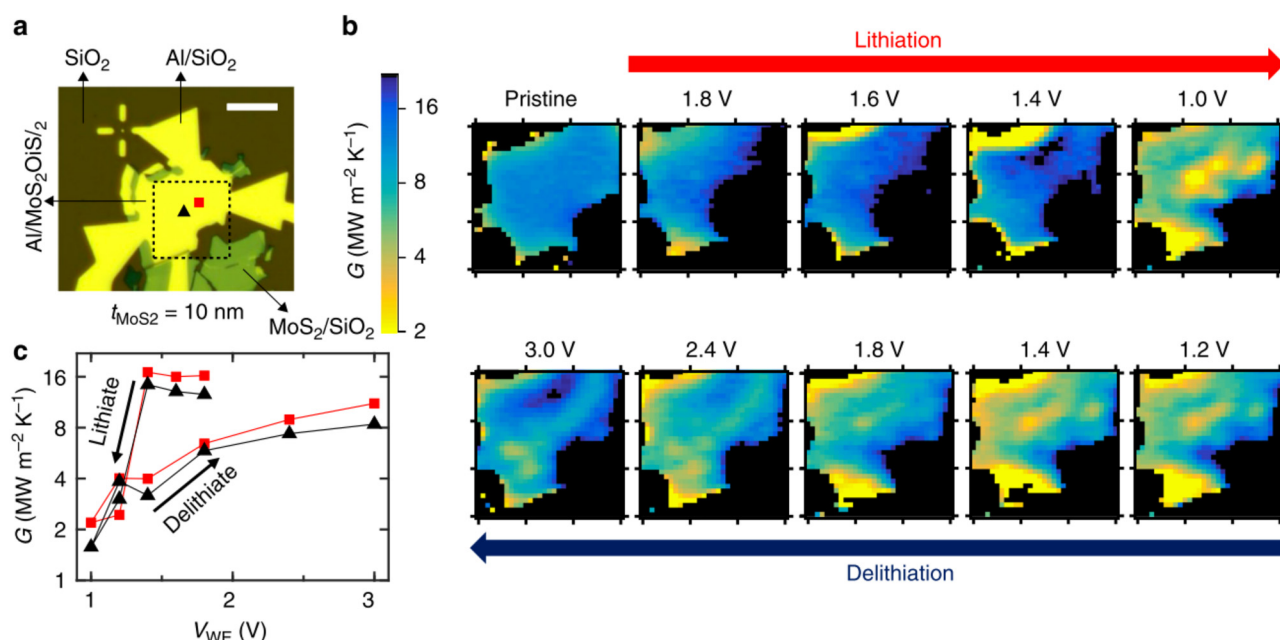
FIG. 10. (a) Optical micrograph of a 10 nm MoS_2 device. The square region marked by the dotted lines is where the conductance images were performed via TDTR. (b) Thermal conductance images of the MoS_2 device at different stages of the lithium intercalation process over a single electrochemical cycle. Micrographs are taken at a constant potential during the lithiation (1.8–1.0 V) and delithiation (1.2 V–3.0 V) processes. (c) Thermal conductance vs voltage for two points probed over the cycling process. The two points are indicated in (a) by the black triangle and red square. Reproduced with permission from Sood *et al.*, Nat. Commun. **9**, 4510 (2018). Copyright 2018 Nature Publishing Group.

discussed the significance of the "lateral" resolution associated with TDTR and FDTR and its importance for this abstraction of the technique. The lateral resolution, however, is inherently limited by diffraction using conventional lenses and objectives. Oil immersion objectives with numerical apertures greater than unity, as well as artificially engineered metamaterials,[131] offer unique, untapped avenues in achieving resolution beyond the diffraction limit. Indeed, a push toward shorter wavelengths offers an increase in resolution, but the associated thermoreflectance coefficients at these wavelengths must also be taken into consideration.[132] Beyond the associated lateral resolution in thermoreflectance techniques, the "depth profiling" applicability leaves much to be studied. We discussed extensively the characteristic length scales in Sec. II, and how the fundamental probing volume associated with TDTR and FDTR techniques cannot extend beyond the spot size in the cross-plane direction. Even so, the high modulation frequencies associated with these techniques limit these volumes to even nearer to the surface, limiting the available information to be garnered. SSTR offers promising capabilities, as probing volumes are typically on the order of the spot size. For polycrystalline systems, the analysis becomes increasingly difficult as a result of the multitude of orientations probed but will, however, provide a better fundamental understanding of variations of thermal conductivity in the through-plane direction. Combined with the excellent lateral resolution associated with the technique, the implementation will work on the basis of deriving

a three-dimensional description of the thermal conductivity for a provided region.

In Sec. IV, we expand on the capabilities of TDTR and FDTR, departing from the transient and modulated heating regime and entering into a steady-state regime in SSTR.[59] SSTR has a multitude of advantages as compared to the aforementioned techniques, as discussed below.

IV. STEADY-STATE THERMOREFLECTANCE

A recent experimental extension of these thermoreflectance-based metrologies is the SSTR technique.[59] In both TDTR and FDTR, an amplitude-modulated heat source induces a both steady-state and modulated temperature rise in a material.[133] The premise of TDTR and FDTR is to capture the modulated temperature rise so that the steady-state component is ignored.[5] In contrast, the premise of SSTR is to capture this steady-state temperature rise.

A. Principles of operation

The principles of SSTR are discussed extensively in the work of Braun *et al.*,[59] and thus, only the basics will be presented here. The configuration of SSTR is akin to that of FDTR, where an amplitude-modulated pump heats the specimen of interest, while the probe monitors the thermoreflectance. A key difference between the two, however, is the frequency of modulation of the pump. In

FDTR, these modulation frequencies are typically on the order of kilohertz to megahertz, where the phase lag between the pump and probe signals is compared to the heat diffusion equation to extract properties of interest. Example FDTR data are shown in Fig. 11, where the phase lag between pump and probe is presented for fused silica, sapphire, boron arsenide, and diamond.[118] Indeed, a significant phase lag is present at these modulation frequencies for materials of low thermal conductivity, i.e., in fused silica and sapphire. For BAs and diamond, on the other hand, the pump and probe remain in-phase with one another until ∼1 MHz. This occurs as a result of the highly conductive nature of these materials, as a steady-state regime is maintained until such high modulation frequencies are reached. Contrarily, for materials less conductive by nature, the phase lag as measured by the probe is indicative of a lack of steady-state regime. Thus, the premise of SSTR is to perform measurements at lower modulation frequencies (<1 kHz) to capitalize on the steady-state temperature rise in these material systems.

Several advantages arise as a result of performing these thermal conductivity measurements at lower modulation frequencies in the steady-state regime as compared to conventional TDTR and FDTR techniques. Typically, the penetration depth, and therefore the probing volume, of the latter two is on the order of several hundred nanometers due to the transient nature of the heating event.[70] This primarily enhances sensitivity to the cross-plane properties of the material system. Contrarily, at modulation frequencies typically used in an SSTR configuration, the penetration depth approaches that of the spot size (cf. Fig. 2) and is fundamentally sensitive to all components of the thermal conductivity tensor for a given material system. Additionally, the use of thin transducers generally enhances sensitivity to properties of the underlying media in SSTR, where sensitivity to the transducer

thickness, thermal conductivity, and interfacial resistance at the transducer/substrate interface are less as compared to TDTR and FDTR. Finally, transient techniques are fundamentally sensitive to the thermal effusivity of bulk materials at conventional modulation frequencies. The steady-state temperature profile, on the other hand, is solely dependent on the thermal conductivity and can be determined independently from the volumetric heat capacity.

B. Implementation

The implementation of SSTR is nearly identical to that of FDTR and will, therefore, not be discussed in depth. A pump of sufficient power should be utilized so as to induce a steady-state temperature rise at the sample surface—for high thermal conductivity materials, this may be as much as 1 W depending on the spot size. Modulation of the pump can be achieved through a variety of methods, either internally to the laser source or externally via an electro-optic or acousto-optic modulator, or a mechanical chopper. The mechanical chopper is preferable due to the high damage thresholds, as generally larger powers are used as compared to TDTR and FDTR. Prior to being combined with the probe, a portion of the pump is directed into a photodetector to extract the magnitude of the pump modulation, ΔP. The rest of the pump power is reflected by a cold mirror and directed to the sample surface. The probe is split into two paths for the implementation of a balanced photodetector scheme, which greatly enhances signal-to-noise at the pump modulation frequencies. After passing through the cold mirror and focused through the objective lens along with the pump, the reflected probe signal is directed to a balanced photodetector with a path-matched reference beam, minimizing common noise in the probe.

There are two approaches to performing an SSTR measurement: (1) by using a lock-in amplifier (LIA) to monitor changes in reflectance as the pump power is systematically increased or (2) by using a periodic waveform analyzer (PWA) to extract both the pump and probe waveforms to extract the thermal conductivity. The extracted signals can be related by the equation

$$\left(\frac{\Delta V}{V \Delta P}\right) = \gamma \left(\frac{\Delta T(\kappa)}{\Delta |Q|}\right), \tag{5}$$

where ΔV is the magnitude of the probe signal, V is the probe DC signal, ΔP is the magnitude of the pump signal, and $\Delta T(\kappa)/\Delta |Q|$ is calculated using the thermal model. γ is a proportionality constant that encompasses the thermoreflectance at the sample surface, differences in objective magnifications and losses, as well as any differences associated with the electronics. Ultimately, it relates the associated changes in the magnitude of the pump and probe to the temperature excursion for a given heat flux at the sample surface. Typically, γ is extracted via the use of a calibration sample, whose thermal conductivity is known from other metrologies. Knowledge of γ is paramount in SSTR, and thus to account for any variations in transducer film quality during deposition processes, a reference specimen should be placed near to the specimen of interest during the deposition of the transducer to confirm the proportionality constant.
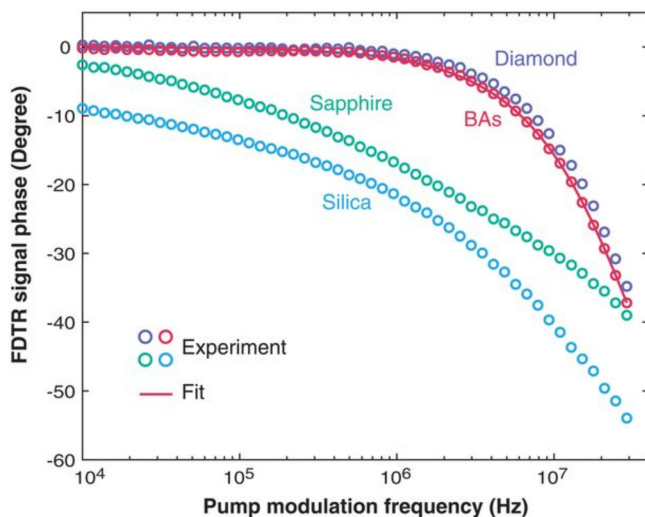
FIG. 11. Representative FDTR signal phase as a function of the pump modulation frequency measured on a BAs crystal, diamond, sapphire, and fused silica. Reprinted with permission from Tian *et al.*, Science **361**, 582–585 (2018). Copyright 2018 AAAS.

C. Measurements

Example SSTR data in the two configurations are shown in Fig. 12. Specifically, Fig. 12(a) shows change in probe photodetector voltage ($\Delta V/V$) as a function of the pump photodetector voltage (ΔP) using the LIA approach. Linear trends in the data are observed for a wide range of thermal conductivities, from that of a-SiO$_2$ to that of diamond. The slope of the data are fit to the heat diffusion equation to extract thermal conductivity, again independently of volumetric heat capacity. Using the PWA approach is much more simplified, as just the pump and probe waveforms for a given pump power need to be acquired. Example pump waveforms for Al on a-SiO$_2$ and Si are shown in Fig. 12(b). Note that a larger pump magnitude is observed on Si as opposed to a-SiO$_2$, due to the increased pump power necessary to induce a steady-state temperature rise of similar magnitude. This is evidenced by the probe waveforms, shown in Fig. 12(c). Due to the low thermal conductivity of a-SiO$_2$, a steady-state regime is not achieved until near the end of the heating event, whereas steady-state is reached nearly instantly in the case of Si due to its highly conductive nature. With knowledge of the pump and probe magnitudes, Eq. (5) can be used to extract the thermal conductivity of the two substrates. Summarized in Fig. 12(d) are the thermal conductivities of materials measured in the study. SSTR is capable of measuring materials with a wide range of thermal conductivities and has been demonstrated in the range of 1–2000 W m^{-1} K^{-1}, independent of the volumetric heat capacity. While currently SSTR has not been applied to systems with thermal conductivities less than 1 W m^{-1} K^{-1}, in principle, there is no limitation to extending SSTR to this regime of low thermal conductivity materials.

D. Summary and future directions for SSTR

In this section, we provide a brief overview of the steady-state based thermoreflectance metrology, SSTR.[59] While TDTR and

FDTR are contingent on the modulated temperature response, the analysis in SSTR is greatly simplified. At low modulation frequencies, the steady-state thermoreflectance response is dominated by the thermal conductivity, independently of the volumetric heat capacity. Additionally, this ensures that the depth of penetration is on the order of the spot size, larger than that of TDTR and FDTR, but smaller than the permissible sample dimensions in bulk techniques, such as laser flash.[71] Thus, power permitting, SSTR allows for the attainment of length scales not captured by current optical techniques, both transient and steady-state, allowing for a broader spectrum of specimen lengths to be measured.

SSTR has shown to be an excellent method to characterize the thermal conductivity for a variety of material systems. Yet, the newness of the technique allows for the potential for a variety of upgrades. For one, the technique relies on a single low modulation frequency to extract the thermal conductivity. This is contingent on the characterization of the calibration coefficient, γ, to be able to relate heat flux to a temperature rise at the sample surface. Potentially, this can be remediated by modulating at higher frequencies in an FDTR-like approach, where sensitivity to the thermal effusivity of the material system is gained over simply the thermal conductivity. In this manner, γ and its requirement can be remediated. Beyond the requirement of the calibration coefficient, the technique lends itself to a variety of implementations that cannot currently be reached by traditional implementations of TDTR or FDTR. As discussed earlier, the characteristic probing volume associated with SSTR is governed by the $1/e^2$ pump/probe radii. Thus, so long as the spot size can be tuned from the typical several micrometers to several hundreds of micrometers in a controlled manner, the associated probing volumes can be tuned as well. As a result, systems in which interfaces are "buried" have a larger potential for being characterized. As an example, vertical diodes are generally fabricated with through-plane dimensions on the order of several micrometers to several tens of micrometers, a
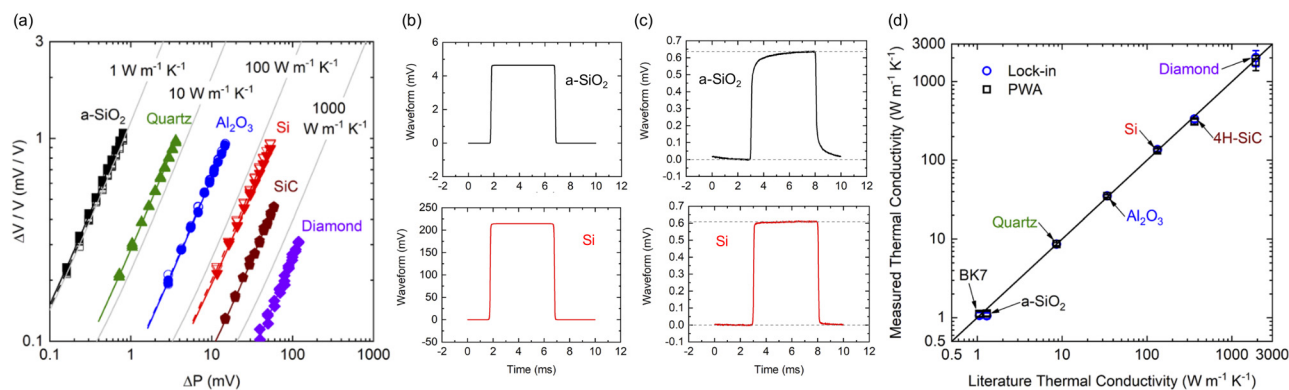
FIG. 12. (a) Experimental data for SSTR: Change in probe photodetector voltage ($\Delta V/V$) vs change in pump detector voltage (ΔP) shown for a glass slide (squares), a BK7 glass window (open squares), a quartz wafer (triangles), a sapphire wafer (circles), a sapphire window (open circles), a silicon wafer (inverted triangles), a silicon window (open inverted triangles), a 4H-SiC wafer (pentagons), and a diamond substrate (diamonds). Gray lines show the predicted slopes for materials having thermal conductivities 1, 10, 100, and 1000 W m^{-1} K^{-1}. (b) Pump and (c) probe waveforms for a-SiO$_2$ and Si, used for extracting the thermal conductivity via the PWA approach. (d) Measured vs literature thermal conductivity. Results are shown for analyses via the LIA (open circles) and PWA (open squares) approaches. Reprinted with permission from Braun *et al.*, Rev. Sci. Instrum. **90**, 024905 (2019). Copyright 2019 AIP Publishing LLC.[59]

parameter that must be optimized for associated breakdown voltages.[134–138] By tuning the spot size, sensitivities to different properties of interest, namely, the thermal conductivities of layers and the associated conductances between them, can be altered to extract these relevant parameters. Additionally, barrier coating systems for gas-turbine engines consist of a top-layer environmental barrier coating (EBC), typically on the order of $100\,\mu$m.[139,140] The thermomechanical stability of the turbine blade is contingent on the silicon bond coat applied between the turbine blade and the top EBC coat. SSTR offers the capability of characterizing this delicate interface, power permitting, making it a potential diagnostic tool for aerospace applications.

In Sec. V, the implementation of the aforementioned transient thermoreflectance techniques is shown in sample configurations that lack a typical transducer layer.

V. THERMOREFLECTANCE TECHNIQUES WITHOUT THE USE OF A THIN FILM OPTOTHERMAL TRANSDUCER

Thermoreflectance techniques have shown their vast range of capabilities in the measurement of thermal properties of material systems, including interfacial conductances,[141–143] thermal conductivities and their associated anisotropies,[144,145] and volumetric heat capacities.[19,146] While nondestructive, typical implementations of these techniques require the deposition of a thin metal transducer to capitalize on the larger thermoreflectance signals associated with these materials.[132,147] Additionally, due to the small optical skin depth associated with metals over a range of wavelengths,[86] analysis using a surface heating event is invoked and greatly simplified compared to volumetric heating events. Furthermore, the thermoreflectance of these metal transducers is linearly proportional to temperature under small perturbations, whereas semiconductors have an additional component to their thermoreflectivity, excited carrier populations, which convolutes the thermoreflectance signal. However, the deposition of a thin metal film inherently modifies the specimen of interest and introduces an additional interfacial thermal resistance that may not be ideal for realization of the underlying thermal properties.

A. Implementation

Initially, transducerless measurements via thermoreflectance techniques showed strong applicability in the ion implantation community. Smith et al.[75] first exemplified the application of an FDTR configuration at a fixed modulation frequency of 100 kHz for the characterization of annealed and nonannealed ion implanted silicon via photothermal reflectance. Specifically, they monitor this signal for boron implanted Si for doses ranging from 10^{11} to 10^{15} B$^+$ ions cm^{-2} at an accelerating voltage of 175 keV. They observe an increase in the measured thermal-wave signal with increasing ion dose, suggestive of an overall decrease in the thermal conductivity of the underlying Si, consistent with the more recent work by Scott et al.[149] Several other works applied the technique for the characterization of semiconductor wafers,[76–82,84] although no quantitative discussion regarding the thermal properties is provided.

The experimental extrapolation for transducerless thermoreflectance measurements is identical to that of conventional ones—only

considerations in the analysis must be taken into account. However, the choice of the pump and probe wavelengths, if possible, should be chosen such that the heating event induced by the pump and optical penetration depth of the probe are near surface, which greatly simplifies the overall analysis. Yang et al.[150] have extensively modeled optical absorption in measurements for TDTR and FDTR, considering the pump as a volumetric heating source. Briefly, they solve the heat conduction equation in the frequency domain, assuming an exponentially-decaying heat generation term. Both the absorption depths of the pump, δ_0, and probe, δ_1, must be considered in this analysis. If δ_0 and δ_1 are not known for a given material system, then the effective optical penetration depth, $\delta_{\text{eff}} = \delta_0 + \delta_1$, can be applied as a fitting parameter given additional known values in a given material system. We emphasize that direct-probing bulk specimens is primarily sensitive to the associated in-plane transport of the system, as opposed to its cross-plane component with the addition of a metal transducer.[92] This occurs as a result of the generally larger temperature gradients associated with the in-plane direction as opposed to the cross-plane direction for measurements performed at modulation frequencies in which the thermal penetration depth is much smaller than the spot size. Specific examples of the implementation of transducerless thermoreflectance measurements are presented below.

B. Measurements

To date, few measurements have been performed without a transducer via thermoreflectance techniques. Khafizov et al.[148] exemplified the possibility of performing transducerless measurements on proton-irradiated silicon using TDTR. Specifically, they employ a probe offset approach to monitor the phase lag as a function of pump/probe separation,[151–153] similar to approaches for measuring the anisotropic thermal conductivity of materials via a beam-offset approach.[144,154] Figure 13 shows representative data and best fits for polished and proton-irradiated Si at 125 K.[148] The difference in phase lag between the two specimens is suggestive of a change in the thermal conductivity as a result of the irradiation process. Indeed, they recover values of $210 \pm 24\,\text{W m}^{-1}\,\text{K}^{-1}$ and $137 \pm 4\,\text{W m}^{-1}\,\text{K}^{-1}$ for polished and proton-irradiated specimens, respectively, at 125 K. While departing from the conventional TDTR approach (concentrically aligned pump/probe beams), the analysis offered by Khafizov et al. exemplifies the ability to employ advanced TDTR techniques that account for optical absorption so as to extract thermal parameters of interest in the absence of a metal transducer.

Furthermore, Yang et al.[150] performed FDTR measurements applying the transducerless formulation to 490 nm amorphous silicon (a-Si) on fused silica and silicon systems, employing cw pump and probe lasers at 785 and 532 nm, respectively. This implementation ensures that $\delta_0 > \delta_1$. Both the thermal conductivity of the a-Si top layer and δ_{eff} are chosen as fitting parameters. Figure 14(a) shows the data and best fit for the a-Si/SiO$_2$ system when the volumetric heating term is not considered. Evidently, the model fails to capture the measured data when fitting for the thermal conductivity of the a-Si top layer. With the implementation of the depth-dependent heating term, however, the model is in excellent agreement with the data, as shown in Fig. 14(b). It is
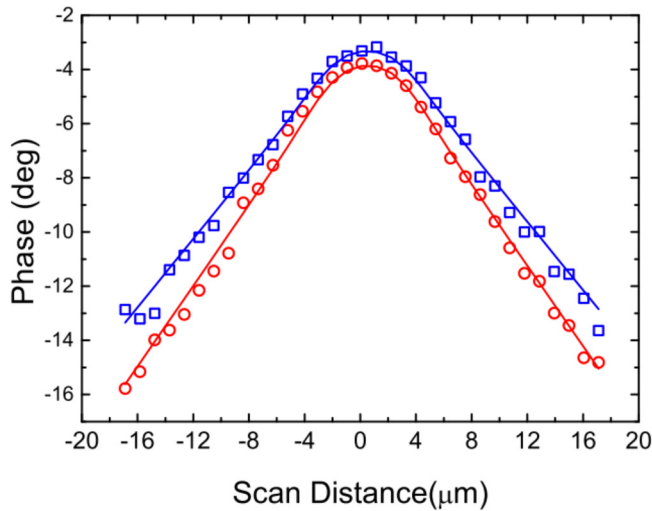
FIG. 13. Time-resolved thermal-wave microscopy data of polished and proton-irradiated silicon used to extract their associated thermal conductivities in the absence of a metal transducer at 125 K. Blue squares and red triangles are data for the polished and proton-irradiated silicon specimens, respectively, while the solid lines are best fits to the data. Reprinted with permission from Khafizov et al., Nucl. Instrum. Methods Phys. Res. B **325**, 11–14 (2014). Copyright 2014 Elsevier.[148]

important to note, however, that both the thermal conductivity of the a-Si layer and δ_{eff} are chosen as fitting parameters, where 1.3 ± 0.1 W m^{-1} K^{-1} and 296 ± 10 nm are extracted, respectively. The thermal conductivity of the a-Si layer agrees well with the literature,[155–157] but fitting for δ_{eff} leaves much to be desired.

Wang et al.[92] extended measurements in the absence of a metal transducer to a variety of bulk semiconductors to extract their associated thermal conductivities using a combined FDTR/TDTR approach. Because TDTR is contingent on the use of pulsed lasers, pump/probe delay times, pump modulation frequencies, and photon energies can be judiciously chosen such that the thermoreflectance signal is dominated by thermal carriers and not that of excited electronic carriers. In their implementation, Wang et al.[92] perform pulsed FDTR measurements at a fixed pump/probe delay time to extract the radial thermal conductivity in Si, GaAs, and InSb. Most importantly, the optical penetration depth is not used as a fitting parameter in this implementation but is rather taken from the literature for the given pump and probe wavelengths.[86]

The importance of pump/probe delay time choice is also emphasized, as earlier delay times are indicative of the excited carrier contribution to reflectance in addition to the contribution from temperature. Example data and best fits from Wang et al.[92] on GaAs at 200 ps and 5 ns are shown in Fig. 15. In the case of 200 ps, the model fails to capture the acquired data, attributed to the additional contributions to thermoreflectivity via excited carriers. At 5 ns, however, far from the associated relaxation time of these carriers, the extracted data and model agree very well with one another, and a thermal conductivity of GaAs that agrees well
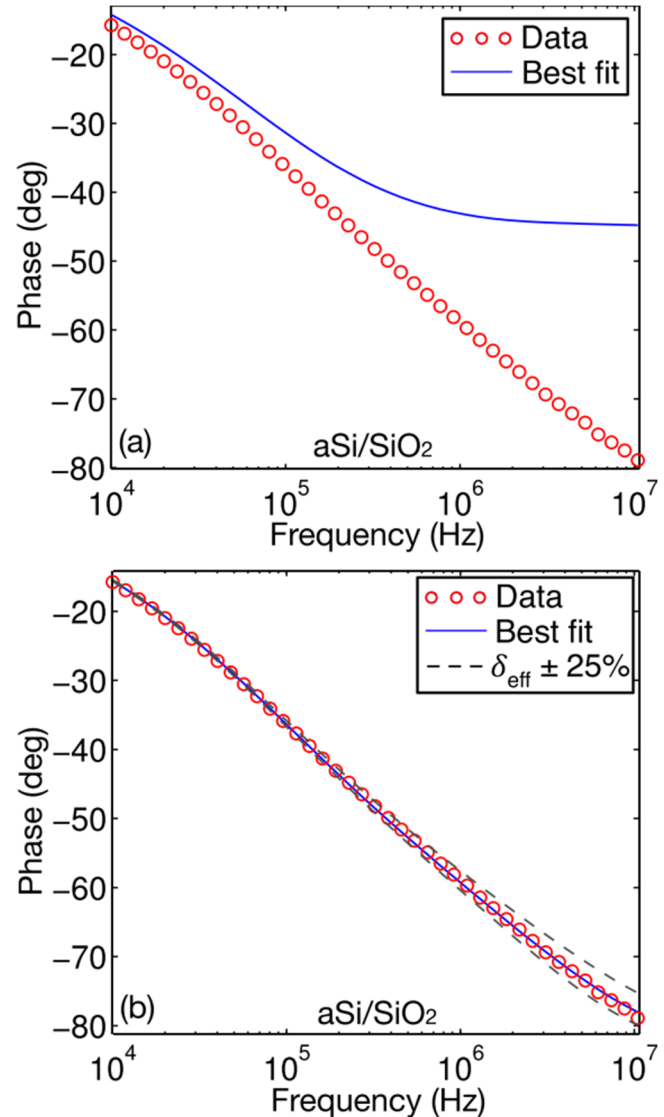
FIG. 14. (a) Data and best fit for a 490 nm aSi on a fused silica specimen assuming a surface heating event. The model and data do not agree. (b) Data and best fit of the specimen when the thermal conductivity of the aSi and effective penetration depth, δ_{eff}, are chosen as fitting parameters. Good agreement is found between the model and data. Reproduced with permission from Yang et al., J. Appl. Phys. **119**, 095107 (2016). Copyright 2016 AIP Publishing LLC.

with the literature is recovered. However, despite performing transducerless thermoreflectance measurements on semiconducting materials, with emphasis on the implementation of a volumetric heating source in the analysis, the similarity in optical and heat penetration depths in GaAs and InSb at the pump wavelength reduces the analysis to that of a surface heating event. Thus, for materials in which these two metrics are comparable to one
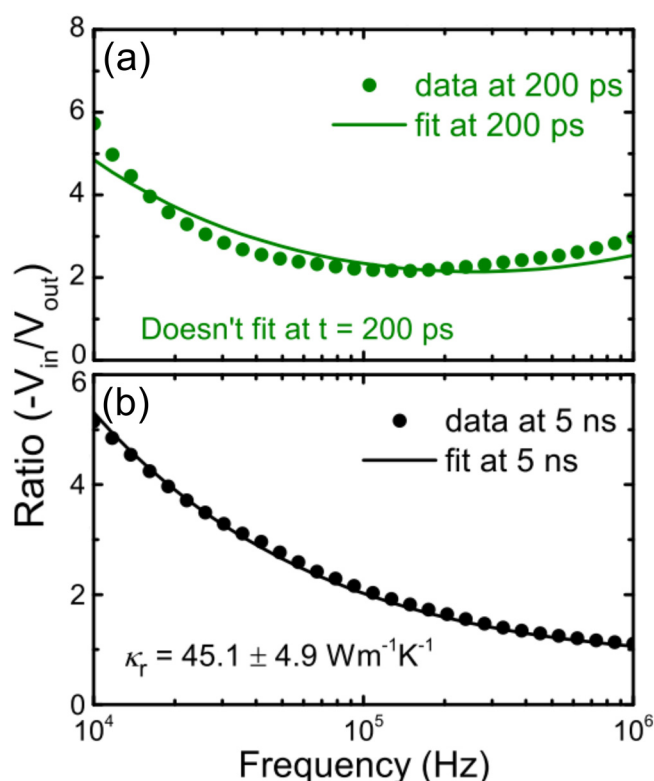
FIG. 15. Pulsed FDTR measurements of GaAs at fixed pump/probe delay times of (a) 200 ps and (b) 5 ns. The data do not fit at 200 ps but fit well at 5 ns, attributed to the excited carrier contribution to the thermoreflectance signal at early delay times. Reproduced with permission from Wang *et al.*, Rev. Sci. Instrum. **87**, 094902 (2016). Copyright 2016 AIP Publishing LLC.

another, the analysis is greatly simplified as few modifications are required for the procedure.

C. Summary and future directions for employing thermoreflectance techniqueswithout the use of a thin film optothermal transducer

Measurements via thermoreflectance techniques in a transducerless configuration have shown promising results. With knowledge of the optical constants of the material system being probed, analysis using the heat diffusion model that accounts for volumetric heating and probing can be readily implemented. Nonetheless, adjusting system parameters such that near-surface heating events are induced is ideal, as with a typical metal transducer. Thus, a push toward UV-based pump/probe systems that ensure near-surface absorption is promising, as the analysis is greatly simplified and not obfuscated by the associated pump/probe optical penetration depths and their contributions to the thermoreflectance signal.

Practically, a pump/probe laser system with variable wavelengths should be implemented, so as to allow for a variety of absorption depths for a given material system. While we have

emphasized that reducing the optical absorption depth greatly simplifies the analysis, increasing this parameter offers the potential to enhanced sensitivity to underlying media that cannot be probed during a near-surface heating event. While we have not discussed the implementation of SSTR in a transducerless configuration, the implementation is akin to that of TDTR and FDTR, as discussed earlier. Modeling should be done in a similar fashion; however, SSTR fundamentally differs from the latter two in that it encapsulates the thermal conductivity tensor, whereas primarily the in-plane components are probed in the two transient techniques. A variety of avenues can thus be undertaken, offering the possibility for novel measurements to better understand device design and fabrication.

VI. CONCLUSION

Thermoreflectance-based techniques have shown good applicability for the characterization of the thermal properties of a variety of material systems. Due to the inherently micrometer-scale spot sizes associated with focusing through high numerical-aperture objective lenses, diffraction limited spots can be achieved, vastly improving the spatial resolution of the measurement system. For materials with inhomogeneities or phase contrasts, rastering the specimen greatly increases throughput and yields insight into novel mechanisms of thermal transport. Nonetheless, at typical modulation frequencies, the probing volumes in TDTR and FDTR are inherently limited due to the modulated nature of the pump heating event. SSTR offers exciting new possibilities, probing depths on the order of the spot size while independently measuring thermal conductivity from volumetric heat capacity. Because the probing volume is on the order of the spot size, depths from several micrometers to millimeters, power permitting, can be achieved, allowing for an understanding of the thermal conductivity of the underlying media at these depths. A push should, however, be made toward UV-based thermoreflectance systems. Currently, modification of specimens via the deposition of a metal transducer can be alleviated by probing the specimen directly. However, the inherent absorption of the pump and probe and their contributions to thermoreflectance must be accounted for. UV-based systems ensure near surface absorption, greatly simplifying the analysis and allowing for a greater slew of materials to be accessed. Overall, thermoreflectance offers exciting capabilities in the field of thermophysical metrologies, and the unique characterization of the fundamental heat transfer mechanisms using the variations described in this perspective will drive the micro- and nanomaterial industries.

REFERENCES

[1]R. Rosei and D. W. Lynch, "Thermomodulation spectra of Al, Au, and Cu," Phys. Rev. B **5**, 3883–3894 (1972).

[2]G. L. Eesley, "Observation of nonequilibrium electron heating in copper," Phys. Rev. Lett. **51**, 2140–2143 (1983).

[3]C. A. Paddock and G. L. Eesley, "Transient thermoreflectance from thin metal films," J. Appl. Phys. **60**, 285–290 (1986).

[4]J. Opsal, A. Rosencwaig, and D. L. Willenborg, "Thermal-wave detection and thin-film thickness measurements with laser beam deflection," Appl. Opt. **22**, 3169 (1983).

[5]D. G. Cahill, "Analysis of heat flow in layered structures for time-domain thermoreflectance," Rev. Sci. Instrum. **75**, 5119–5122 (2004).

[6]A. J. Schmidt, R. Cheaito, and M. Chiesa, "A frequency-domain thermoreflectance method for the characterization of thermal properties," Rev. Sci. Instrum. **80**, 094901 (2009).

[7]D. G. Cahill, W. K. Ford, K. E. Goodson, G. D. Mahan, A. Majumdar, H. J. Maris, R. Merlin, and S. R. Phillpot, "Nanoscale thermal transport," J. Appl. Phys. **93**, 793–818 (2003).

[8]A. Schmidt, "Pump-probe thermoreflectance," Annu. Rev. Heat Transfer **16**, 159–181 (2013).

[9]D. G. Cahill, P. V. Braun, G. Chen, D. R. Clarke, S. Fan, K. E. Goodson, P. Keblinski, W. P. King, G. D. Mahan, A. Majumdar, H. J. Maris, S. R. Phillpot, E. Pop, and L. Shi, "Nanoscale thermal transport. II. 2003–2012," Appl. Phys. Rev. **1**, 11305 (2014).

[10]R. Cheaito, J. T. Gaskins, M. E. Caplan, B. F. Donovan, B. M. Foley, A. Giri, J. C. Duda, C. J. Szwejkowski, C. Constantin, H. J. Brown-Shaklee, J. F. Ihlefeld, and P. E. Hopkins, "Thermal boundary conductance accumulation and interfacial phonon transmission: Measurements and theory," Phys. Rev. B **91**, 73 (2015).

[11]R. B. Wilson and D. G. Cahill, "Limits to Fourier theory in high thermal conductivity single crystals," Appl. Phys. Lett. **107**, 203112 (2015).

[12]J. C. Duda, P. E. Hopkins, Y. Shen, and M. C. Gupta, "Thermal transport in organic semiconducting polymers," Appl. Phys. Lett. **102**, 251912 (2013).

[13]J. C. Duda, P. E. Hopkins, Y. Shen, and M. C. Gupta, "Exceptionally low thermal conductivities of films of the fullerene derivative PCBM," Phys. Rev. Lett. **110**, 015902 (2013).

[14]R. M. Costescu, D. G. Cahill, F. H. Fabreguette, Z. A. Sechrist, and S. M. George, "Ultra-low thermal conductivity in W/Al$_2$O$_3$ nanolaminates," Sci. Rep. **303**, 989–991 (2004).

[15]R. M. Costescu, D. G. Cahill, F. H. Fabreguette, Z. A. Sechrist, S. M. George, P. Keblinski, and P. Zschack, "Ultra-low thermal conductivity in W/Al$_2$O$_3$ nanolaminates," Sci. Rep. **303**, 989–990 (2004).

[16]M. D. Losego, I. P. Blitz, R. A. Vaia, D. G. Cahill, and P. V. Braun, "Ultralow thermal conductivity in organoclay nanolaminates synthesized via simple self-assembly," Nano Lett. **13**, 2215–2219 (2013).

[17]X. Wang, C. D. Liman, N. D. Treat, M. L. Chabinyc, and D. G. Cahill, "Ultralow thermal conductivity of fullerene derivatives," Phys. Rev. B **88**, 075310 (2013).

[18]A. Giri, J. P. Niemelä, C. J. Szwejkowski, M. Karppinen, and P. E. Hopkins, "Reduction in thermal conductivity and tunable heat capacity of inorganic/organic hybrid superlattices," Phys. Rev. B **93**, 024201 (2016).

[19]J. Liu, J. Zhu, M. Tian, X. Gu, A. Schmidt, and R. Yang, "Simultaneous measurement of thermal conductivity and heat capacity of bulk and thin film materials using frequency-dependent transient thermoreflectance method," Rev. Sci. Instrum. **84**, 034902 (2013).

[20]M. N. Luckyanova, J. Garg, K. Esfarjani, A. Jandl, M. T. Bulsara, A. J. Schmidt, A. J. Minnich, S. Chen, M. S. Dresselhaus, Z. Ren, E. A. Fitzgerald, and G. Chen, "Coherent phonon heat conduction in superlattices," Science **338**, 936–939 (2012).

[21]M. N. Luckyanova, J. A. Johnson, A. A. Maznev, J. Garg, A. Jandl, M. T. Bulsara, E. A. Fitzgerald, K. A. Nelson, and G. Chen, "Anisotropy of the thermal conductivity in GaAs/AlAs superlattices," Nano Lett. **13**, 3973–3977 (2013).

[22]J. Ravichandran, A. K. Yadav, R. Cheaito, P. B. Rossen, A. Soukiassian, S. J. Suresha, J. C. Duda, B. M. Foley, C.-H. Lee, Y. Zhu, A. W. Lichtenberger, J. E. Moore, D. A. Muller, D. G. Schlom, P. E. Hopkins, A. Majumdar,

R. Ramesh, and M. A. Zurbuchen, "Crossover from incoherent to coherent phonon scattering in epitaxial oxide superlattices," Nat. Mater. **13**, 168–172 (2013).

[23]R. Cheaito, C. S. Gorham, A. Misra, K. Hattar, and P. E. Hopkins, "Thermal conductivity measurements via time-domain thermoreflectance for the characterization of radiation induced damage," J. Mater. Res. **30**, 1403–1412 (2015).

[24]R. Cheaito, K. Hattar, J. T. Gaskins, A. K. Yadav, J. C. Duda, T. E. Beechem, J. F. Ihlefeld, E. S. Piekos, J. K. Baldwin, A. Misra, and P. E. Hopkins, "Thermal flux limited electron Kapitza conductance in copper-niobium multilayers," Appl. Phys. Lett. **106**, 093114 (2015).

[25]P. Dongmo, Y. Zhong, P. Attia, C. Bomberger, R. Cheaito, J. F. Ihlefeld, P. E. Hopkins, and J. Zide, "Enhanced room temperature electronic and thermoelectric properties of the dilute bismuthide InGaBiAs," J. Appl. Phys. **112**, 093710 (2012).

[26]P. Chen, N. A. Katcho, J. P. Feser, W. Li, M. Glaser, O. G. Schmidt, D. G. Cahill, N. Mingo, and A. Rastelli, "Role of surface-segregation-driven intermixing on the thermal transport through planar Si/Ge superlattices," Phys. Rev. Lett. **111**, 115901 (2013).

[27]R. Cheaito, J. C. Duda, T. E. Beechem, K. Hattar, J. F. Ihlefeld, D. L. Medlin, M. A. Rodriguez, M. J. Campion, E. S. Piekos, and P. E. Hopkins, "Experimental investigation of size effects on the thermal conductivity of silicon-germanium alloy thin films," Phys. Rev. Lett. **109**, 195901 (2012).

[28]P. E. Hopkins, "Thermal transport across solid interfaces with nanoscale imperfections: Effects of roughness, disorder, dislocations, and bonding on thermal boundary conductance," ISRN Mech. Eng. **2013**, 682586.

[29]P. E. Hopkins, J. C. Duda, C. W. Petz, and J. A. Floro, "Controlling thermal conductance through quantum dot roughening at interfaces," Phys. Rev. B **84**, 035438 (2011).

[30]J. C. Duda and P. E. Hopkins, "Systematically controlling Kapitza conductance via chemical etching," Appl. Phys. Lett. **100**, 111602 (2012).

[31]P. E. Hopkins and P. M. Norris, "Thermal boundary conductance response to a change in Cr/Si interfacial properties," Appl. Phys. Lett. **89**, 131909 (2006).

[32]P. E. Hopkins, P. M. Norris, R. J. Stevens, T. Beechem, and S. Graham, "Influence of interfacial mixing on thermal boundary conductance across a chromium/silicon interface," J. Heat Transfer **130**, 62402 (2008).

[33]P. E. Hopkins, J. C. Duda, S. P. Clark, C. P. Hains, T. J. Rotter, L. M. Phinney, and G. Balakrishnan, "Effect of dislocation density on thermal boundary conductance across GaSb/GaAs interfaces," Appl. Phys. Lett. **98**, 161913 (2011).

[34]Z. Su, J. P. Freedman, J. H. Leach, E. A. Preble, R. F. Davis, and J. A. Malen, "The impact of film thickness and substrate surface roughness on the thermal resistance of aluminum nitride nucleation layers," J. Appl. Phys. **113**, 213502 (2013).

[35]Z. Su, L. Huang, F. Liu, J. Freedman, L. M. Porter, R. F. Davis, and J. A. Malen, "Layer-by-layer thermal conductivities of the Group III nitride films in blue/green light emitting diodes," Appl. Phys. Lett. **100**, 201106 (2012).

[36]J. P. Freedman, X. Yu, R. F. Davis, A. J. Gellman, and J. A. Malen, "Thermal interface conductance across metal alloy-dielectric interfaces," Phys. Rev. B **93**, 035309 (2016).

[37]B. M. Foley, S. C. Hernández, J. C. Duda, J. T. Robinson, S. G. Walton, and P. E. Hopkins, "Modifying surface energy of graphene via plasma-based chemical functionalization to tune thermal and electrical transport at metal interfaces," Nano Lett. **15**, 4876–4882 (2015).

[38]P. E. Hopkins, M. Baraket, E. V. Barnat, T. E. Beechem, S. P. Kearney, J. C. Duda, J. T. Robinson, and S. G. Walton, "Manipulating thermal conductance at metal-graphene contacts via chemical functionalization," Nano Lett. **12**, 590–595 (2012).

[39]M. D. Losego, M. E. Grady, N. R. Sottos, D. G. Cahill, and P. V. Braun, "Effects of chemical bonding on heat transport across interfaces," Nat. Mater. **11**, 502–506 (2012).

[40]J. Yang, E. Ziade, C. Maragliano, R. Crowder, X. Wang, M. Stefancich, M. Chiesa, A. K. Swan, and A. J. Schmidt, "Thermal conductance imaging of graphene contacts," J. Appl. Phys. **116**, 023515 (2014).

[41]S. Majumdar, J. A. Sierra-Suarez, S. N. Schiffres, W. L. Ong, C. F. Higgs, A. J. McGaughey, and J. A. Malen, "Vibrational mismatch of metal leads controls thermal conductance of self-assembled monolayer junctions," Nano Lett. **15**, 2985–2991 (2015).

[42]Z. Ge, D. G. Cahill, and P. V. Braun, "Thermal conductance of hydrophilic and hydrophobic interfaces," Phys. Rev. Lett. **96**, 186101 (2006).

[43]Z. Tian, A. Marconnet, and G. Chen, "Enhancing solid-liquid interface thermal transport using self-assembled monolayers," Appl. Phys. Lett. **106**, 211602 (2015).

[44]H. Harikrishna, W. A. Ducker, and S. T. Huxtable, "The influence of interface bonding on thermal transport through solid-liquid interfaces," Appl. Phys. Lett. **102**, 251606 (2013).

[45]J. Park, J. Huang, W. Wang, C. J. Murphy, and D. G. Cahill, "Heat transport between Au nanorods, surrounding liquids, and solid supports," J. Phys. Chem. C **116**, 26335–26341 (2012).

[46]J. A. Tomko, D. H. Olson, A. Giri, J. T. Gaskins, B. F. Donovan, S. M. O'Malley, and P. E. Hopkins, "Nanoscale wetting and energy transmission at solid/liquid interfaces," Langmuir **35**, 2106–2114 (2019).

[47]K. T. Regner, J. P. Freedman, and J. A. Malen, "Advances in studying phonon mean free path dependent contributions to thermal conductivity," Nanoscale Microscale Thermophys. Eng. **19**, 183–205 (2015).

[48]K. T. Regner, S. Majumdar, and J. A. Malen, Instrumentation of broadband frequency domain thermoreflectance for measuring thermal conductivity accumulation functions," Rev. Sci. Instrum. **84**, 064901 (2013).

[49]K. T. Regner, D. P. Sellan, Z. Su, C. H. Amon, A. J. McGaughey, and J. A. Malen, "Broadband phonon mean free path contributions to thermal conductivity measured using frequency domain thermoreflectance," Nat. Commun. **4**, 1640–1647 (2013).

[50]K. T. Regner, L. C. Wei, and J. A. Malen, "Interpretation of thermoreflectance measurements with a two-temperature model including non-surface heat deposition," J. Appl. Phys. **118**, 235101 (2015).

[51]J. P. Freedman, J. H. Leach, E. A. Preble, Z. Sitar, R. F. Davis, and J. A. Malen, "Universal phonon mean free path spectra in crystalline semiconductors at high temperature," Sci. Rep. **3**, 2963 (2013).

[52]A. J. Minnich, J. A. Johnson, A. J. Schmidt, K. Esfarjani, M. S. Dresselhaus, K. A. Nelson, and G. Chen, "Thermal conductivity spectroscopy technique to measure phonon mean free paths," Phys. Rev. Lett. **107**, 095901 (2011).

[53]K. M. Hoogeboom-Pot, J. N. Hernandez-Charpak, X. Gu, T. D. Frazer, E. H. Anderson, W. Chao, R. W. Falcone, R. Yang, M. M. Murnane, H. C. Kapteyn, and D. Nardi, "A new regime of nanoscale thermal transport: Collective diffusion increases dissipation efficiency," Proc. Natl. Acad. Sci. U.S.A. **112**, 4846–4851 (2015).

[54]M. E. Siemens, Q. Li, R. Yang, K. A. Nelson, E. H. Anderson, M. M. Murnane, and H. C. Kapteyn, "Quasi-ballistic thermal transport from nanoscale interfaces observed using ultrafast coherent soft X-ray beams," Nat. Mater. **9**, 26–30 (2010).

[55]L. Zeng, K. C. Collins, Y. Hu, M. N. Luckyanova, A. A. Maznev, S. Huberman, V. Chiloyan, J. Zhou, X. Huang, K. A. Nelson, and G. Chen, "Measuring phonon mean free path distributions by probing quasiballistic phonon transport in grating nanostructures," Sci. Rep. **5**, 17131 (2015).

[56]P. E. Hopkins, "Effects of electron-boundary scattering on changes in thermoreflectance in thin metal films undergoing intraband excitations," J. Appl. Phys. **105**, 93517 (2009).

[57]P. E. Hopkins, "Influence of electron-boundary scattering on thermoreflectance calculations after intra- and interband transitions induced by short-pulsed laser absorption," Phys. Rev. B **81**, 35413 (2010).

[58]P. E. Hopkins, "Thermoreflectance dependence on Fermi surface electron number density perturbations," Appl. Phys. Lett. **96**, 041901 (2010).

[59]J. L. Braun, D. H. Olson, J. T. Gaskins, and P. E. Hopkins, "A steady-state thermoreflectance method to measure thermal conductivity," Rev. Sci. Instrum. **90**, 024905 (2019).

[60]J. Opsal and A. Rosencwaig, "Thermal and plasma wave depth profiling in silicon," Appl. Phys. Lett. **47**, 498–500 (1985).

[61]T. Heilpern, M. Manjare, A. O. Govorov, G. P. Wiederrecht, S. K. Gray, and H. Harutyunyan, "Determination of hot carrier energy distributions from inversion of ultrafast pump-probe reflectivity measurements," Nat. Commun. **9**, 1853 (2018).

[62]E. L. Radue, J. A. Tomko, A. Giri, J. L. Braun, X. Zhou, O. V. Prezhdo, E. L. Runnerstrom, J. P. Maria, and P. E. Hopkins, "Hot electron thermoreflectance coefficient of gold during electron-phonon nonequilibrium," ACS Photonics **5**, 4880–4887 (2018).

[63]T. Tanaka, A. Harata, and T. Sawada, "Subpicosecond surface-restricted carrier and thermal dynamics by transient reflectivity measurements," J. Appl. Phys. **82**, 4033–4038 (1997).

[64]A. J. Sabbah and D. M. Riffe, "Measurement of silicon surface recombination velocity using ultrafast pump-probe reflectivity in the near infrared," J. Appl. Phys. **88**, 6954–6956 (2000).

[65]A. J. Sabbah and D. M. Riffe, "Femtosecond pump-probe reflectivity study of silicon carrier dynamics," Phys. Rev. B **66**, 165217 (2002).

[66]H. Carslaw and J. C. Jaeger, *Conduction of Heat in Solids*, 2nd ed. (Oxford University Press, 1959). pp. 109–112.

[67]A. J. Schmidt, X. Chen, and G. Chen, "Pulse accumulation, radial heat conduction, and anisotropic thermal conductivity in pump-probe transient thermoreflectance," Rev. Sci. Instrum. **79**, 114902 (2008).

[68]Y. K. Koh and D. G. Cahill, "Frequency dependence of the thermal conductivity of semiconductor alloys," Phys. Rev. B **76**, 075207 (2007).

[69]A. Sood, F. Xiong, S. Chen, R. Cheaito, F. Lian, M. Asheghi, Y. Cui, D. Donadio, K. E. Goodson, and E. Pop, "Quasi-ballistic thermal transport across MoS_2 thin films," Nano Lett. **19**, 2434–2442 (2019).

[70]J. L. Braun and P. E. Hopkins, "Upper limit to the thermal penetration depth during modulated heating of multilayer thin films with pulsed and continuous wave lasers: A numerical study," J. Appl. Phys. **121**, 175107 (2017).

[71]W. J. Parker, R. J. Jenkins, C. P. Butler, and G. L. Abbott, "Flash method of determining thermal diffusivity, heat capacity, and thermal conductivity," J. Appl. Phys. **32**, 1679–1684 (1961).

[72]G. Tessier, M. Bardoux, C. Boú, C. Filloy, and D. Fournier, "Back side thermal imaging of integrated circuits at high spatial resolution," Appl. Phys. Lett. **90**, 171112 (2007).

[73]D. Kendig, K. Yazawa, and A. Shakouri, "Hyperspectral thermoreflectance imaging for power devices," in *Annual IEEE Semiconductor Thermal Measurement, Modeling, & Management Symposium (Semi-Therm)* (IEEE, 2017), pp. 204–207.

[74]A. Rosencwaig, "Thermal-wave imaging," Science **218**, 223–228 (1982).

[75]W. Smith, M. W. Taylor, and J. Schuur, "Ultra-high-resolution dose uniformity monitoring with thermal waves," Proc. SPIE **0530**, 201–214 (1985).

[76]J. Schuur, C. Waters, J. Maneval, N. Tripsis, A. Rosencwaig, M. Taylor, W. L. Smith, L. Golding, and J. Opsal, "Relaxation of ion implant damage on silicon wafers at room temperature measured by thermal waves and double implant sheet resistance," Nucl. Instrum. Methods Phys. Res. B **21**, 554–558 (1987).

[77]B. J. Kirby, L. A. Larson, and R.-Y. Liang, "Thermal-wave measurements of ion implanted silicon," Nucl. Instrum. Methods Phys. Res. B **21**, 550–553 (1987).

[78]M. A. Wendman and W. L. Smith, "Thermal wave implant dosimetry for process control on product wafers," Nucl. Instrum. Methods Phys. Res. B **21**, 559–562 (1987).

[79]N. Uchitomi, H. Mikami, N. Toyoda, and R. Nii, "Experimental study on the correlation between thermal-wave signals and dopant profiles for silicon-implanted GaAs," Appl. Phys. Lett. **52**, 30–32 (1988).

[80]I. A. Vitkin, C. Christofides, and A. Mandelis, "Laser-induced photothermal reflectance investigation of silicon damaged by arsenic ion implantation: A temperature study," Appl. Phys. Lett. **54**, 2392–2394 (1989).

[81]I. A. Vitkin, C. Christofides, and A. Mandelis, "Photothermal reflectance investigation of processed silicon. II. Signal generation and lattice temperature dependence in ion-implanted and amorphous thin layers," J. Appl. Phys. **67**, 2822–2830 (1990).

[82]C. Christofides, I. A. Vitkin, and A. Mandelis, "Photothermal reflectance investigation of processed silicon. I. Room-temperature study of the induced damage and of the annealing kinetics of defects in ion-implanted wafers," J. Appl. Phys. **67**, 2815–2821 (1990).

[83]L. Pottier, "Micrometer scale visualization of thermal waves by photoreflectance microscopy," Appl. Phys. Lett. **64**, 1618–1619 (1994).

[84]C. Christofides, F. Diakonos, A. Seas, C. Christou, M. Nestoros, and A. Mandelis, "Two-layer model for photomodulated thermoreflectance of semiconductor wafers," J. Appl. Phys. **80**, 1713–1725 (1996).

[85]P. E. Hopkins, J. R. Serrano, L. M. Phinney, S. P. Kearney, T. W. Grasser, and C. T. Harris, "Criteria for cross-plane dominated thermal transport in multilayer thin film systems during modulated laser heating," J. Heat Transfer **132**, 81302 (2010).

[86]E. D. Palik, *Handbook of Optical Constants of Solids* (Academic Press, 1985).

[87]S. Huxtable, D. G. Cahill, V. Fauconnier, J. O. White, and J.-C. Zhao, "Thermal conductivity imaging at micrometre-scale resolution for combinatorial studies of materials," Nat. Mater. **3**, 298–301 (2004).

[88]S. Dilhaire, G. Pernot, G. Calbris, J. M. Rampnoux, and S. Grauby, "Heterodyne picosecond thermoreflectance applied to nanoscale thermal metrology," J. Appl. Phys. **110**, 114314 (2011).

[89]Q. d'Acremont, G. Pernot, J. M. Rampnoux, A. Furlan, D. Lacroix, A. Ludwig, and S. Dilhaire, "High-throughput heterodyne thermoreflectance: Application to thermal conductivity measurements of a Fe-Si-Ge thin film alloy library," Rev. Sci. Instrum. **88**, 074902 (2017).

[90]J. Yang, C. Maragliano, and A. J. Schmidt, "Thermal property microscopy with frequency domain thermoreflectance," Rev. Sci. Instrum. **84**, 104904 (2013).

[91]K. Hatori, N. Taketoshi, T. Baba, and H. Ohta, "Thermoreflectance technique to measure thermal effusivity distribution with high spatial resolution," Rev. Sci. Instrum. **76**, 114901 (2005).

[92]L. Wang, R. Cheaito, J. L. Braun, A. Giri, and P. E. Hopkins, "Thermal conductivity measurements of non-metals via combined time- and frequency-domain thermoreflectance without a metal film transducer," Rev. Sci. Instrum. **87**, 094902 (2016).

[93]J.-C. Zhao, X. Zheng, and D. G. Cahill, "High-throughput diffusion multiples," Mater. Today **8**, 28–37 (2005).

[94]X. Zheng, D. Cahill, P. Krasnochtchekov, R. Averback, and J.-C. Zhao, "High-throughput thermal conductivity measurements of nickel solid solutions and the applicability of the Wiedemann-Franz law," Acta Mater. **55**, 5177–5185 (2007).

[95]A. Sood, R. Cheaito, T. Bai, H. Kwon, Y. Wang, C. Li, L. Yates, T. Bougher, S. Graham, M. Asheghi, M. Goorsky, and K. E. Goodson, "Direct visualization of thermal conductivity suppression due to enhanced phonon scattering near individual grain boundaries," Nano Lett. **18**(6), 3466–3472 (2018).

[96]A. Sood, F. Xiong, S. Chen, H. Wang, D. Selli, J. Zhang, C. J. Mcclellan, J. Sun, D. Donadio, Y. Cui, E. Pop, and K. E. Goodson, "An electrochemical thermal transistor," Nat. Commun. **9**, 4510 (2018).

[97]F. W. Zok, "Ceramic-matrix composites enable revolutionary gains in turbine engine efficiency," Am. Ceram. Soc. Bull. **95**, 22–28 (2016), available at https://ceramics.org/wp-content/bulletin/2016/junejuly16/JuneJuly16Bulletin-ceramic-matrix-composites.pdf.

[98]G. H. Lohnert, H. Nabielek, and W. Schenk, "The fuel element of the HTR-module, a prerequisite of an inherently safe reactor," Nucl. Eng. Des. **109**, 257–263 (1988).

[99]D. G. Martin, "Considerations pertaining to the achievement of high burn-ups in HTR fuel," Nucl. Eng. Des. **213**, 241–258 (2002).

[100]X. Zheng, D. G. Cahill, and J. C. Zhao, "Thermal conductivity imaging of thermal barrier coatings," Adv. Eng. Mater. **7**, 622–626 (2005).

[101]E. López-Honorato, C. Chiritescu, P. Xiao, D. G. Cahill, G. Marsh, and T. Abram, "Thermal conductivity mapping of pyrolytic carbon and silicon carbide coatings on simulated fuel particles by time-domain thermoreflectance," J. Nucl. Mater. **378**, 35–39 (2008).

[102]X. Zhang, L. Hou, A. Ciesielski, and P. Samorì, "2D materials beyond graphene for high-performance energy storage applications," Adv. Energy Mater. **6**, 1600671 (2016).

[103]M. Wang and E. H. Yang, "THz applications of 2D materials: Graphene and beyond," Nano-Struct. Nano-Objects **15**, 107–113 (2018).

[104]F. Wang, Z. Wang, Q. Wang, F. Wang, L. Yin, K. Xu, Y. Huang, and J. He, "Synthesis, properties and applications of 2D non-graphene materials," Nanotechnology **26**, 292001 (2015).

[105]M. Chen, H. Nam, S. Wi, L. Ji, X. Ren, L. Bian, S. Lu, and X. Liang, "Stable few-layer MoS₂ rectifying diodes formed by plasma-assisted doping," Appl. Phys. Lett. **103**, 142110 (2013).

[106]M. S. Choi, D. Qu, D. Lee, X. Liu, K. Watanabe, T. Taniguchi, and W. J. Yoo, "Lateral MoS₂ p-n junction formed by chemical doping for use in high-performance optoelectronics," ACS Nano **8**, 9332–9340 (2014).

[107]P. Zhao, D. Kiriya, A. Azcatl, C. Zhang, M. Tosun, Y. S. Liu, M. Hettick, J. S. Kang, S. McDonnell, S. Kc, J. Guo, K. Cho, R. M. Wallace, and A. Javey, "Air stable p-doping of WSe₂ by covalent functionalization," ACS Nano **8**, 10808–10814 (2014).

[108]E. Pop, V. Varshney, and A. K. Roy, "Thermal properties of graphene: Fundamentals and applications," MRS Bull. **37**, 1273–1281 (2012).

[109]W. Jang, Z. Chen, W. Bao, C. N. Lau, and C. Dames, "Thickness-dependent thermal conductivity of encased graphene and ultrathin graphite," Nano Lett. **10**, 3909–3913 (2010).

[110]J. H. Seol, I. Jo, A. L. Moore, L. Lindsay, Z. H. Aitken, M. T. Pettes, X. Li, Z. Yao, R. Huang, D. Broido, N. Mingo, R. S. Ruoff, and L. Shi, "Two-dimensional phonon transport in supported graphene," Science **328**, 213–216 (2010).

[111]S. Ghosh, W. Bao, D. L. Nika, S. Subrina, E. P. Pokatilov, C. N. Lau, and A. A. Balandin, "Dimensional crossover of thermal transport in few-layer graphene," Nat. Mater. **9**, 555–558 (2010).

[112]M. M. Sadeghi, I. Jo, and L. Shi, "Phonon-interface scattering in multilayer graphene on an amorphous support," Proc. Natl. Acad. Sci. U.S.A. **110**, 16321–16326 (2013).

[113]Y.-G. Choi, D.-G. Jeong, H. I. Ju, C. J. Roh, G. Kim, B. S. Mun, T. Y. Kim, S.-W. Kim, and J. S. Lee, "Covalent-bonding-induced strong phonon scattering in the atomically thin WSe2 layer," Sci. Rep. **9**, 7612 (2019); e-print arXiv:1812.02383.

[114]D. B. Brown, W. Shen, X. Li, K. Xiao, D. B. Geohegan, and S. Kumar, "Spatial mapping of thermal boundary conductance at metal-molybdenum diselenide interfaces," ACS Appl. Mater. Interfaces **11**, 14418–14426 (2019).

[115]S. V. Garimella, L. T. Yeh, and T. Persoons, "Thermal management challenges in telecommunication systems and data centers," IEEE Trans. Compon. Packaging Manuf. Technol. **2**, 1307–1316 (2012).

[116]J. R. Olson, R. O. Pohl, J. W. Vandersande, A. Zoltan, T. R. Anthony, and W. F. Banholzer, "Thermal conductivity of diamond between 170 and 1200 K and the isotope effect," Phys. Rev. B **47**, 14850–14856 (1993).

[117]G. A. Slack, "Thermal conductivity of pure and impure silicon, silicon carbide, and diamond," J. Appl. Phys. **35**, 3460–3466 (1964).

[118]F. Tian, B. Song, X. Chen, N. K. Ravichandran, Y. Lv, K. Chen, S. Sullivan, J. Kim, Y. Zhou, T. H. Liu, M. Goni, Z. Ding, J. Sun, G. Amila, G. U. Gamage, H. Sun, H. Ziyaee, S. Huyan, L. Deng, J. Zhou, A. J. Schmidt, S. Chen, C. W. Chu, P. Y. Huang, D. Broido, L. Shi, G. Chen, and Z. Ren, "Unusual high thermal conductivity in boron arsenide bulk crystals," Science **361**, 582–585 (2018).

[119]S. Li, Q. Zheng, Y. Lv, X. Liu, X. Wang, P. Y. Huang, D. G. Cahill, and B. Lv, "High thermal conductivity in cubic boron arsenide crystals," Science **361**, 579–581 (2018).

[120]J. S. Kang, M. Li, H. Wu, H. Nguyen, and Y. Hu, "Experimental observation of high thermal conductivity in boron arsenide," Science **361**, 575–578 (2018).

[121]G. Wehmeyer, T. Yabuki, C. Monachon, J. Wu, and C. Dames, "Thermal diodes, regulators, and switches: Physical mechanisms and potential applications," Appl. Phys. Rev. **4**, 041304 (2017).

[122]X. Gou, H. Ping, Q. Ou, H. Xiao, and S. Qing, "A novel thermoelectric generation system with thermal switch," Appl. Energy **160**, 843–852 (2015).

[123]X. Zhang and L. D. Zhao, "Thermoelectric materials: Energy conversion between heat and electricity," J. Materiomics **1**, 92–105 (2015).

[124]Y. Yan and J. A. Malen, "Periodic heating amplifies the efficiency of thermoelectric energy conversion," Energy Environ. Sci. **6**, 1267–1273 (2013).

[125]A. Sood, E. Pop, M. Asheghi, and K. E. Goodson, "The heat conduction renaissance," in *2018 17th IEEE Intersociety Conference on Thermal and Thermomechanical Phenomena in Electronic Systems (ITherm)* (IEEE, 2018), pp. 1396–1402.

[126]J. A. Tomko, A. Pena-Francesch, H. Jung, M. Tyagi, B. D. Allen, M. C. Demirel, and P. E. Hopkins, "Tunable thermal transport and reversible thermal conductivity switching in topologically networked bio-inspired materials," Nat. Nanotechnol. **13**, 959–964 (2018).

[127]B. M. Foley, H. J. Brown-Shaklee, J. C. Duda, R. Cheaito, B. J. Gibbons, D. Medlin, J. F. Ihlefeld, and P. E. Hopkins, "Thermal conductivity of nanograined $SrTiO_3$ thin films," Appl. Phys. Lett. **101**, 231908 (2012).

[128]B. F. Donovan, B. M. Foley, J. F. Ihlefeld, J.-P. Maria, and P. E. Hopkins, "Spectral phonon scattering effects on the thermal conductivity of nano-grained barium titanate," Appl. Phys. Lett. **105**, 82907 (2014).

[129]M. A. Py and R. R. Haering, "Structural destabilization induced by lithium intercalation in MoS_2 and related compounds," Can. J. Phys. **61**, 76–84 (1983).

[130]F. Xiong, H. Wang, X. Liu, J. Sun, M. Brongersma, E. Pop, and Y. Cui, "Li intercalation in MoS_2: In situ observation of its dynamics and tuning optical and electrical properties," Nano Lett. **15**, 6777–6784 (2015).

[131]X. Zhang and Z. Liu, "Superlenses to overcome the diffraction limit," Nat. Mater. **7**, 435–441 (2008).

[132]R. B. Wilson, B. A. Apgar, L. W. Martin, and D. G. Cahill, "Thermoreflectance of metal transducers for optical pump-probe studies of thermal properties," Opt. Express **20**, 28829–28838 (2012).

[133]J. L. Braun, C. J. Szwejkowski, A. Giri, and P. E. Hopkins, "On the steady-state temperature rise during laser heating of multilayer thin films in optical pump-probe techniques," J. Heat Transfer **140**, 052801 (2018).

[134]D. Disney, H. Nie, A. Edwards, D. Bour, H. Shah, and I. C. Kizilyalli, "Vertical power diodes in bulk GaN," in *Proceedings of the International Symposium on Power Semiconductor Devices and ICs* (IEEE, 2013), pp. 59–62.

[135]I. C. Kizilyalli, A. P. Edwards, O. Aktas, T. Prunty, and D. Bour, "Vertical power p-n diodes based on bulk GaN," IEEE Trans. Electron Devices **62**, 414–422 (2015).

[136]J. Flicker and R. Kaplar, "Design optimization of GaN vertical power diodes and comparison to Si and SiC," in *2017 IEEE 5th Workshop on Wide Bandgap Power Devices and Applications (WiPDA)* (Sandia National Laboratories, 2017), pp. 31–38.

[137]L. Yates, G. P. S. Graham, S. Usami, K. Nagamatsu, Y. Honda, and H. Amano, "Electrical and thermal analysis of vertical GaN-on-GaN PN diodes," in *Proceedings of the 17th InterSociety Conference on Thermal and Thermomechanical Phenomena in Electronic Systems, ITherm 2018* (IEEE, 2018), pp. 831–837.

[138]V. I. Nikolaev, S. I. Stepanov, A. E. Romanov, and V. E. Bougrov, "Gallium oxide," in *Single Crystals of Electronic Materials*, edited by R. Fornari (Elsevier, 2019), pp. 487–521.

[139]B. T. Richards, M. R. Begley, and H. N. Wadley, "Mechanisms of ytterbium monosilicate/mullite/silicon coating failure during thermal cycling in water vapor," J. Am. Ceramic Soc. **98**, 4066–4075 (2015).

[140]B. T. Richards, K. A. Young, F. de Francqueville, S. Sehr, M. R. Begley, and H. N. Wadley, "Response of ytterbium disilicate-silicon environmental barrier coatings to thermal cycling in water vapor," Acta Mater. **106**, 1–14 (2016).

[141]R. J. Stevens, A. N. Smith, and P. M. Norris, "Measurement of thermal boundary conductance of a series of metal-dielectric interfaces by the transient thermoreflectance technique," J. Heat Transfer **127**, 315 (2005).

[142]B. C. Gundrum, D. G. Cahill, and R. S. Averback, "Thermal conductance of metal-metal interfaces," Phys. Rev. B **72**, 245426 (2005).

[143]H.-K. Lyeo and D. G. Cahill, Thermal conductance of interfaces between highly dissimilar materials," Phys. Rev. B **73**, 144301 (2006).

[144]J. P. Feser, J. Liu, and D. G. Cahill, "Pump-probe measurements of the thermal conductivity tensor for materials lacking in-plane symmetry," Rev. Sci. Instrum. **85**, 104903 (2014).

[145]V. V. Medvedev, J. Yang, A. J. Schmidt, A. E. Yakshin, R. W. Van De Kruijs, E. Zoethout, and F. Bijkerk, "Anisotropy of heat conduction in Mo/Si multi-layers," J. Appl. Phys. **118**, 085101 (2015).

[146]C. Wei, X. Zheng, D. G. Cahill, and J.-C. Zhao, "Invited article: Micron resolution spatially resolved measurement of heat capacity using dual-frequency time-domain thermoreflectance," Rev. Sci. Instrum. **84**, 71301 (2013).

[147]Y. Wang, J. Y. Park, Y. K. Koh, and D. G. Cahill, "Thermoreflectance of metal transducers for time-domain thermoreflectance," J. Appl. Phys. **108**, 043507 (2010).

[148]M. Khafizov, C. Yablinsky, T. R. Allen, and D. H. Hurley, "Measurement of thermal conductivity in proton irradiated silicon," Nucl. Instrum. Methods Phys. Res. B **325**, 11–14 (2014).

[149]E. A. Scott, K. Hattar, C. M. Rost, J. T. Gaskins, M. Fazli, C. Ganski, C. Li, T. Bai, Y. Wang, K. Esfarjani, M. Goorsky, and P. E. Hopkins, "Phonon scattering effects from point and extended defects on thermal conductivity studied via ion irradiation of crystals with self-impurities," Phys. Rev. Mater. **2**, 095001 (2018).

[150]J. Yang, E. Ziade, and A. J. Schmidt, "Modeling optical absorption for thermoreflectance measurements," J. Appl. Phys. **119**, 095107 (2016).

[151]D. H. Hurley and M. K. Fig, "Parametric study of thermal interface resistance using laser-based thermal wave imaging," J. Appl. Phys. **104**, 123703 (2008).

[152]D. H. Hurley, O. B. Wright, O. Matsuda, and S. L. Shinde, Time resolved imaging of carrier and thermal transport in silicon," J. Appl. Phys. **107**, 3091 (2010).

[153]M. Khafizov and D. H. Hurley, "Measurement of thermal transport using time-resolved thermal wave microscopy," J. Appl. Phys. **110**, 083525 (2011).

[154]J. P. Feser and D. G. Cahill, "Probing anisotropic heat transport using time-domain thermoreflectance with offset laser spots," Rev. Sci. Instrum. **83**, 104901 (2012).

[155]P. B. Allen and J. L. Feldman, "Thermal conductivity of glasses: Theory and applications to amorphous Si," Phys. Rev. Lett. **62**, 645–648 (1989).

[156]D. G. Cahill, H. E. Fischer, T. Klitsner, E. T. Swartz, and R. O. Pohl, "Thermal conductivity of thin films: Measurements and understanding," J. Vac. Sci. Technol. A **7**, 1259–1266 (1989).

[157]J. L. Braun, C. H. Baker, A. Giri, M. Elahi, K. Artyushkova, T. E. Beechem, P. M. Norris, Z. C. Leseman, J. T. Gaskins, and P. E. Hopkins, Size effects on the thermal conductivity of amorphous silicon thin films," Phys. Rev. B **93**, 140201 (2016).